NTNU – Trondheim
Norwegian University of
Science and Technology

Pore pressure prediction ahead of the drill bit using Borehole Seismic Data.

Rufino Kacimbombo David

Petroleum Geosciences
Submission date: December 2014
Supervisor: Egil Tjåland, IPT
Co-supervisor: Richard Birchwood, Schlumberger

Norwegian University of Science and Technology
Department of Petroleum Engineering and Applied Geophysics

NTNU-Trondheim
Norwegian University of
Science and Tecnology.

Pore Pressure Prediction Ahead of the Bit Using Borehole Seismic Data.

Rufino David.

Earth Sciences and Petroleum Engineering
Supervisor: Egil djalan, IPT; Richard Birchwood, Schlumberger
Submission date: December 2014

Department of Petroleum Engineering and Applied Geophysics
Norwegian University of Science and Technology.

Summary

Knowledge of the formation pore pressure is fundamental to maintaining safety and control of the borehole during drilling operations. Non-hydrostatic pressures can cause blowouts and borehole instability and when they are properly managed the cost of drilling can be significantly reduced [1].

In this thesis pore pressure was inferred "below the drill bit" from synthetically generated borehole seismic data. The formation properties used in the study were based loosely on well log data from the Gulf of Mexico. A hypothetical 100 m thick sedimentary column with horizontal layers was constructed from this data. A synthetic seismic waveform produced by a standard (Ricker wavelet) source and recorded by a single hypothetical receiver at the top of the column was inverted for velocity, bulk density and layer thickness below the receiver. Only upgoing waves were used in the inversion. In practice upgoing and downgoing waves are often separated during processing.

Because the solution is non-unique, the inversion was subject to constraints that could reasonably be applied in a practical setting. The inversion was formulated as a Bayesian problem and solved using the Metropolis algorithm, which generated samples from the posterior probability density function. The inversion scheme was programmed using Wolfram Mathematica® software.

It was found that with the aforementioned constraints, impedance (product of velocity and density) could be obtained with reasonable accuracy and with greater accuracy than the velocity or bulk density individually. The realizations of impedance produced by the simulations were converted to pore pressure using an impedance to pore pressure transform rather than the standard velocity to pore pressure transform. The estimated pore pressure was compared to the "correct" pore pressure computed using the original impedance used to generate the synthetic seismogram. In this way it was possible to analyze the robustness and applicability of the method to drilling operations.

The results showed that the method is capable of reproducing the general trend of pore pressure up to least 50 m below the lowest anchor point. A component of high frequency noise was also observed, but this is usually smoothed out in practice. The study did not explore the potential for inferring pore pressure at greater depths. Four key assumptions/simplifications were made in the course of carrying out the inversion. The first is that layers are horizontal. Secondly, no noise was added to the synthetic seismic data. Thirdly, acoustic attenuation was assumed to be known and constant over the sedimentary column. The sensitivity of results to noisy data and errors or uncertainty in the Q-factor (that governs attenuation) needs to be explored. Finally the statistical distribution of layer thicknesses below the receiver was assumed to be known within a wide margin of error. In practice when drilling a well, the thicknesses of layers below the bit are not known. Consequently it is proposed that statistical information from offset set wells or outcrops could be used. This study shows that even a crude approximation of the actual layer thickness distribution can be sufficient to constrain the profile of impedance below the bit to within reasonable bounds.

Preface

This Master's thesis was written at the Department of Petroleum Engineering and Applied Geophysics at the Norwegian University of Science and Technology, NTNU.

I would like to thank my academic supervisor, Associate Professor Egil Djaland, for his advice and guidance throughout the process and my industry supervisor from Schlumberger, Dr. Richard Birchwood who followed me up and Jon Kleppe who helped to get the internship with Schlumberger.

In addition I would like to thank IPT, Statoil for their support, and Schlumberger Angola Recruiting Manager, Mr. Emerson Jericota, who organized my internship and the Business Development Manager of Schlumberger Geosciences and Petroleum Engineering, Mr. Chitwan Garg, for granting me access to the manpower, office and computing resources of Schlumberger.

The author of this work hereby declares that the work in this thesis is made independently and in accordance to the rules set down by Examination regulations at the Norwegian University of Science and Technology (NTNU), Trondheim.

_____

Rufino David, Luanda 2014

Table of Contents

List of Figures

1. Introduction

Estimating the pore pressure ahead of the bit is a major challenge while drilling. In the process of drilling a well, unexpected deviations from normal pressure can cause several problems and in the worst scenario can result in complete loss of a well due to blowouts or other drilling problems such as hole collapse and stuck pipe. Vertical seismic profiling is a powerful tool from which travel times, wave amplitudes, and reflection coefficient data can be acquired, offering a more detailed seismic view of the subsurface in the vicinity of the borehole than conventional surface seismic data [4] [5]. It is now widely used while drilling to locate the position of a drill-bit on a seismogram, to correct surface seismic data for depth errors, and for geosteering to ensure that subsurface targets are reached. Claims have also been made with respect to its potential to provide estimation of pore pressure ahead of the drill-bit [6].

The objective of this thesis is to predict the pore pressure below a hypothetical seismic receiver recording data at the top of a sedimentary column some 100 m thick. This objective was accomplished by inverting the recorded waveform, subject to suitable constraints, for seismic impedance below the receiver. The inverse problem was formulated using Bayes Theorum. The metropolis algorithm was implemented to draw samples from the posterior probability density function for the unknown parameters. The unknown parameters consisted of the thicknesses, velocities and bulk densities of layers below the bit. Pore pressure was predicted a via-a Bower's-type equation modified to accept impedance as an input instead of velocity. The overburden stress required by this equation was computed from the density profile inferred up to depths below the seismic receiver. This research is expected to have implications for pore pressure prediction, hazard detection, reservoir properties evaluation, and geosteering.

Sonic and bulk density log data from Walker Ridge in the Gulf of Mexico was modified and used to generate synthetic seismograms. The layer properties (Velocity, Density and Impedance) obtained by inverting these seismograms were compared with the known values derived from well data in order to verify the robustness of the method. The cause of overpressure is out of the scope for the present work but a general description about it is provided in the section 2.9

Pore Pressure Prediction Ahead of the Bit Using Borehole Seismic Data.

This thesis constitutes an extension of a student project [4]. The historical review written during the project was incorporated into the thesis.

2. Literature Review

In this section is described the historical review from which the present work is based on.

2.1. Description of Vertical Seismic Profiling

The following sections describe general aspects of Vertical Seismic Profiling, and its importance within geophysics.

2.1.1. The Vertical Seismic Profiling

VSP is a geophysical exploration technique that involves making downhole measurements with a borehole seismic tool of acoustic signals originated from surface seismic sources. Seismic waves are typically generated from controlled explosion, movement caused by vibroseis trucks, or air guns, travelling from the source to the interior of the earth. When reflections take place at layer interfaces, a contrast of acoustic impedance is detected due to difference in velocities and densities between layers [7]; [8]; [9].

During a VSP survey, an array of geophones in the borehole captures downgoing waves that arrive directly from the source and upgoing waves that are reflected from layers below the receivers. Upward and downward propagating waves are separated by processing. Calibration of a continuous velocity log is done using the first recorded arrivals of downgoing waves. Waves propagating upward are processed in a manner similar to reflection seismic data [7]; [8]. A VSP survey makes it possible to relate surface seismic data recorded in time to wellbore data recorded in depth. It can also be used to differentiate primary from secondary events (multiples) and to determine the depths of layers where reflections are generated [8]; [10].

2.1.1.1. Types of VSP Survey

Many different variants of the VSP technique are distinguished by their respective source and receiver geometries.

2.1.1.1.1. Check-shot VSP

The most common type of VSP surveys is the check shot. It is known as a low cost velocity survey and it has been applied since 1940. This technique measures the direct travel time from source to receiver with no reflection along the way. It provides the measurement of seismic velocity near the well and relates seismic time to well depth. This technique provides seismic velocities along the well path and a relation between seismic travel time and well depth. To acquire data, an immobile seismic source is used and a receiver that measure the travel time indication, from the surface to a specific reflector [1] (figure 1).

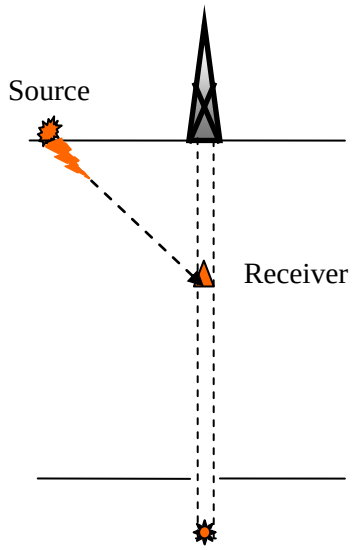

Figure 1. A checkshot VSP survey measuring the direct travel time. Lateral distance between the well and source is exaggerated Modified from Arroyo et al [1].

2.1.1.1.2. Zero Offset VSP

The Zero-offset VSP has been used since 1950. In this technique the source is placed vertically above the receiver and the reflected seismic signal is captured delivering a seismic image below the total depth of the well [1] (figure 2).

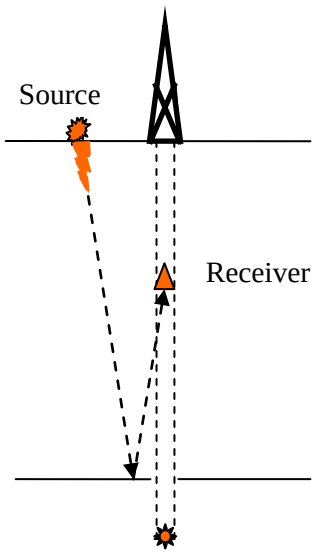

Figgure 2. A Zero-offset VSP survey measuring the two-way travel time Modified from Arroyo et al [1].

2.1.1.1.3. Offset and Walk-Above VSP Surveys

The offset VSP is done by placing a single source far away from the well (figure 3a). The downhole geophones detect reflections emanating from reflectors located away from the wellbore. The walk-above technique is characterised by source application directly over a downhole receiver in a deviated well [1] (figure 3b).

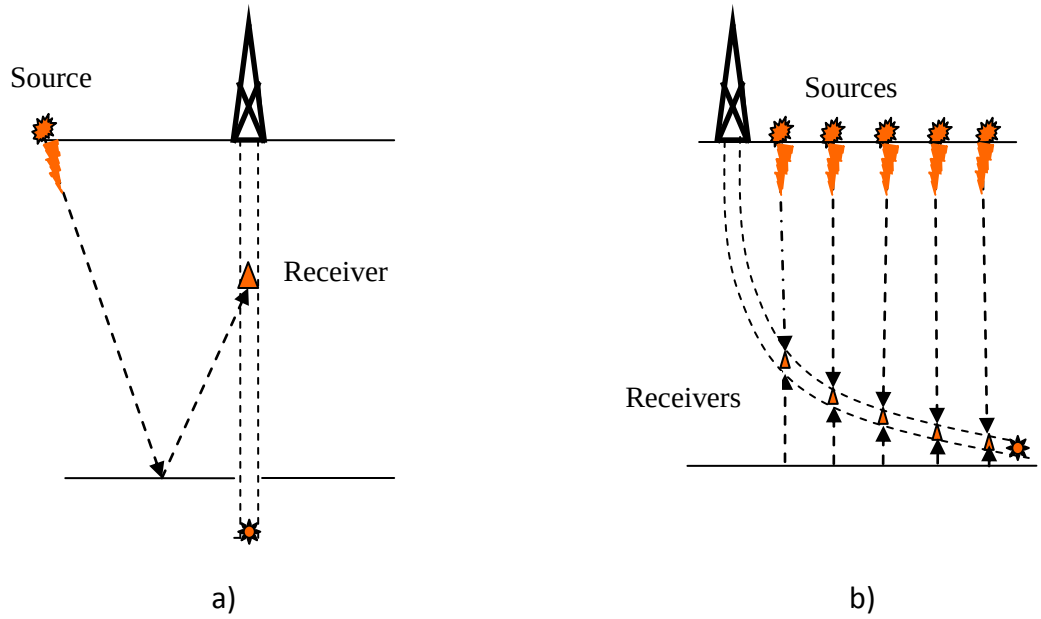

Figure 3. (a) A VPS survey measuring the two-way travel time using Offset VSP; (b) One-way travel time using Walk-above technique Modified from Arroyo et al [1].

2.1.1.1.4. Walk-Away VSP

In the walk-away VSP, a receiver array of five to seven geophones is used. Data is obtained from different surface source locations along a line from the well from which hundred of sources are placed. After data processing an image of the subsurface with a higher resolution than that of a surface seismic survey is generated [1] (figure 4).

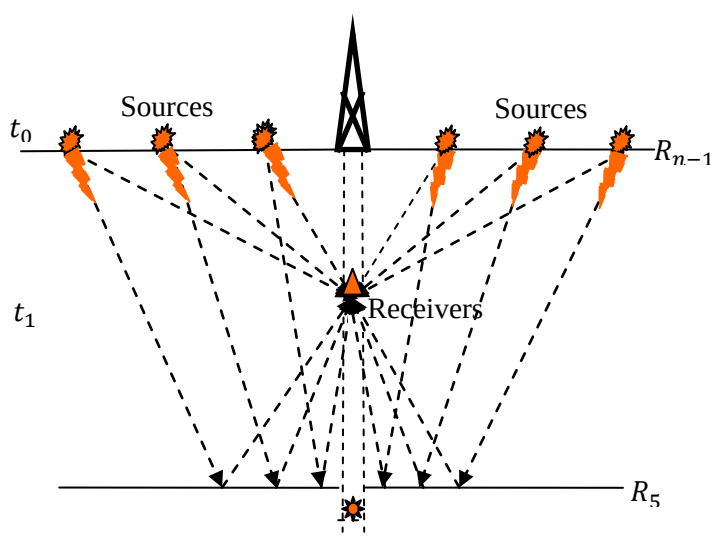

Figure 4. A VPS survey measuring one-way travel time using Walk-away technique Modified from Arroyo et al [1].

2.2. Historical Review of Vertical Seismic Profiling

Vertical Seismic Profile has been recognised as a useful technique within the oil industry due to its ability to enhance surface seismic data [11]. The famous Russian geophysicist Gal'perin and his colleagues revolutionalized VSP. They conducted a great deal of research from the 1960's in the USSR. Their effort was rewarded after two decades; the technique was accepted and became well known in the geophysical industry [8]; [11]. Years after the technique made its way to Europe. In 1970 the VSP made a great impact in the United States because of its ability to look ahead of the drill bit. Refinements in techniques used to invert zero-offset VSP data was a major step forward in enhancing the look-ahead capabilities of VSP surveys. In the East of Texas (US) Pinnacle reefs was successfully located as a subsurface feature [8]. The US geological survey conducted a study for earth investigation over a period of 8 years that utilized VSP [8].

2.3. Current VSP applications and advantages [10].

Information on the depth versus arrival time extracted from the down-going wave-field can be used to locate a drilled section on time-based surface seismic images.

- Depths of layer sequences and boundaries observed in seismic data can be inferred.
- Improved well navigation (geosteering) to ensure that targets identified on seismic data are intersected.
- The down-going and up-going wave-fields show the variation with depth of acoustic properties such as impedance and viscous damping.
- The VSP generated synthetic seismogram provides a clearer reflection profile than that obtained from the sonic logs.
- The direct down-going wave-field can be used to determine velocities which provide insight on rock properties.
- Differentiate between the primaries and multiples of seismic waves.
- The proximity of receivers to the target zone enables VSP data to have a better Signal/Noise ratio and higher resolution than surface seismic data.

- The VSP is a useful technique that helps to get an image of the subsurface interface structure beneath the borehole to predict the depths to reflectors and velocities ahead of the bit [10]; [6].

2.4. Processing of Zero-offset data set

To illustrate the processing of zero-offset VSP consider the data set described by Malinverno et al [2]. The vibrator source exhibited frequencies between 8 and 120 Hz. Harmonics generated by nonlinearities from the vibrator source produced a downgoing wavefield with components of up to 200 Hz (Figure 5a). The semblance deconvolution method adopted by Malinverno et al [2] was used to process the data. This method effectively converted the downgoing wave-field at all receivers to a zero-phase wavelet with an almost constant spectrum in the 10-200 Hz interval. (Figure 5b) shows the reflection response of the earth to the source obtained by deconvolution of the upgoing wave-field Malinverno et al [2].

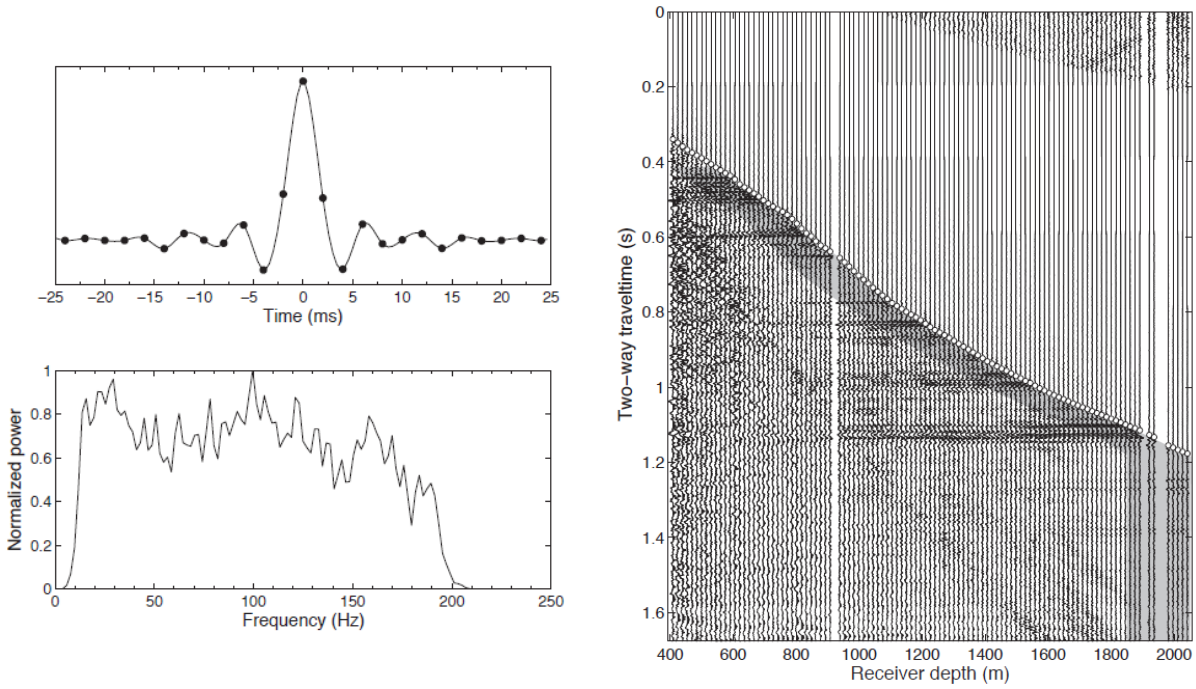

a) b)

Figure 5. Representation of the Zero-offset VSP data. (a) The averaged downgoing wave (Malinverno et al [2]); (b) Spectrum of averaged downgoing wave taken from Malinverno et al [2].

Two-way travel times at each receiver and the portion of the traces used to produce a corridor stack are also shown. By averaging the upgoing traces recorded by the receiver array, a corridor stack was produced. The corridor stack obtained using 10 traces is observed in fig 6. By stacking the data the signal to noise ratio is increased Malinverno et al [2] (figure 6).

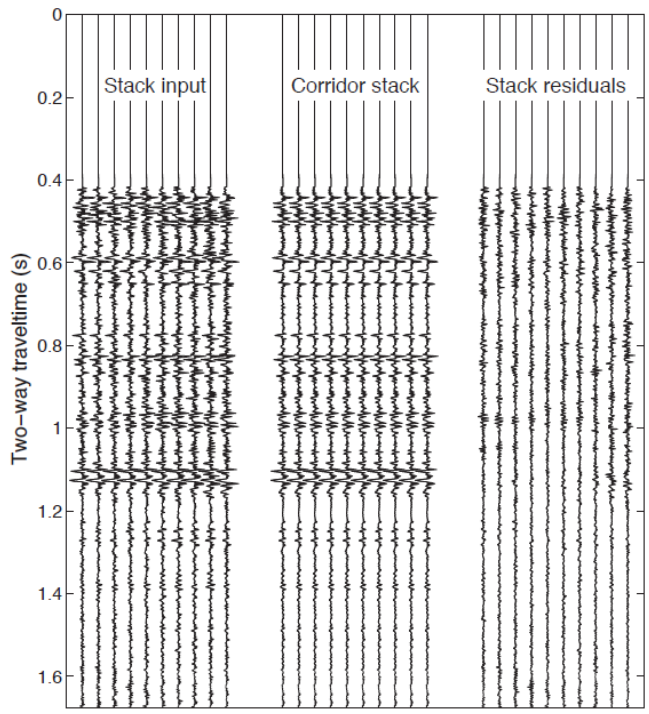

Figure 6. The residual at the Right was computed from the difference between the Stack input at the left and the corridor stack in the middle (Malinverno et al [2]).

2.5. Travel-time and Reflection coefficients

VSP travel time data has traditionally been used to infer seismic velocities between receivers. A simple way to treat this problem is to estimate velocity from VSP first-arrival times [12]. Considering a flat layer example the travel time for a direct arrival from the source to receiver can be computed using Pythagoras' theorem in eqn (1).

$$t_d = \frac{1}{v_0}\sqrt{h^2 + z^2}, \qquad (1)$$

From the example above the travel time for a reflected arrival can be computed as

$$t_r = \frac{1}{v_0}\sqrt{h^2 + (2z_1 - z)^2}, \qquad (2)$$

From equations (1) and (2), velocity can be computed given the travel times and the corresponding layer thicknesses above the bit [12].

Velocity obtained from equations above can offer a considerable amount of uncertainty for many reasons. Inversion of seismic travel time provides a means to reduce the uncertainty and construct a realistic velocity profile [12]. A formula for inverting travel-times was devised by Stewart [13] and is as follows:

$$T(H) = \int_0^H \sqrt{(1 - V_{(z)}^2 (\frac{1}{V_{(H)}^2} - (\frac{dT}{dZ})^2))}\, \frac{dZ}{V_z}, \qquad (3)$$

The reflection coefficient is the ratio of the amplitude of the reflected wave and the amplitude of the incident wave. It can be deduced from vertical seismic profiling which differentiates between upward and downward travelling seismic waves Kennet et al [7]. A simple form of reflection coefficient is given by Duijindam [14] as the following relation:

$$r_i = \frac{Z_{i+1} - Z_i}{Z_{i+1} + Z_i}, \qquad (4)$$

2.6. Theory of Synthetic seismograms

In this study a synthetic seismogram representing upgoing waveforms recorded by a VSP tool was generated. The theory of how to generate a synthetic seismogram from knowledge of the density, velocity and adsorption properties of formations in the subsurface can be found in [15]. Key elements are summarized in this section. Consider a column consisting of N horizontal layers numbered 1, 2, 3, …N from top to bottom. An impulsive signal is generated at the surface producing downgoing and upgoing waves in the top layer [15]. The relation between downgoing and upgoing waves in this layer is given by the following expression:

$$D_1(w) = (1 - R_o U_1(w)) \qquad (5)$$

Definitions of symbols can be found in the Nomenclature section. The Fourier transform of a synthetic seismogram recorded on the surface is defined as the sum of the Fourier transforms of upgoing and downgoing waves, i.e. [15]

$$X(w) = U_1(w) + (1 - R_o U_1(w)) \tag{6}$$

$$= (1 - R_o)\, U_1(w) + 1$$

The ratio of the spectrum of the upcoming wave to the downgoing wave at the top of layer is expressed as

$$Y_i = \frac{U_i}{D_i}, \tag{7}$$

The following recursive expression for Y_i, which includes absorption effects, is given by:

$$Y_i = e^{-2\alpha d_i} e^{-2iwd_i/c_i} \left(\frac{R_i + Y_{i+1}}{1 - R_i Y_{i+1}}\right), \tag{8}$$

Below are the expressions used to compute the absorption coefficient, the phase velocity and the quality factor [15].

$$\alpha(w) = \frac{|W|}{2C_0 Q_0}, \tag{9}$$

$$c(w) = C_0\left(1 - \frac{1}{\pi Q_0} \ln \frac{Y|W|}{W_0}\right)^{-1}, \tag{10}$$

$$Q'(w) = Q_0\left(1 - \frac{1}{\pi Q_0}\right), \tag{11}$$

Using equations (6) through (11), the synthetic seismogram at the surface can be calculated. Detailed information on computation of synthetic seismograms is given in Ganley, [15].

The equations above were implemented in the Walfram Mathematica software and a synthetic seismogram of upgoing wave was computed from the impulsive signal generated at the surface which produced downgoing and upgoing waves in the top layer using equation (5). A synthetic seismogram was recorded on the surface by summing the Fourier transforms of upgoing and downgoing waves as shown in the equation (6). The ratio of the spectrum of the upcoming wave to the downgoing wave at the top of layer was computed from equation (7). The attenuation effect was assumed to be known as a constant for all layers.

2.7. Theory of Inversion

Inversion is a mathematical procedure used to infer the properties or inputs governing the behaviour of a physical system using a mathematical model that relates inferred quantities to observed outputs from the system. Most often the observed data does not provide enough information to enable the unknown parameters to be determined uniquely. Therefore inverse techniques should consider the uncertainties produced by this lack of information. When correctly applied, inversion should narrow the range of possible solutions that are consistent with the data [16]; [17].

A significant effort has been made by scientists over the years to understand the nature of inverse problems. Overdetermined problems were given special attention by Laplace and Gauss while Hadamard introduced the term “ill-posed problems” also known as the “undetermined problem. The 1960s and 1970s were considered to be the golden age for the theory of inverse problems [16]. During this time Keils-Borok and Yanovskaya produced the first application of Monte Carlo theory to derivation of earth models [16].

One way to account for uncertainty in inverse problems is to express the answer as a probability distribution. The application of Bayes method to geophysical inverse problems results in a posterior probability density function (PDF) $p(\mathbf{m}|\mathbf{d}, \mathbf{I})$ of the vector **m** of the model parameters given a vector **d** of measurements and prior information, **I**. The posterior PDF is related to the prior PDF $p(\mathbf{m}, \mathbf{I})$ of model parameters by the formula [16]; [2]:

$$P(\mathbf{m}|\mathbf{d}, \mathbf{I}) \propto p(\mathbf{m}, \mathbf{I})p(\mathbf{d}|\mathbf{m}, \mathbf{I}), \qquad (12)$$

The posterior distribution provides constraints on the model parameters consistent with prior information and with the data. It is the solution of the inverse problem [16].

Inferring the structure of the earth’s interior using seismic data is a mathematically challenging inverse problem [16]. Seismologists have been the pioneers in the development of the theory of inverse problems. The use of prior information to constrain inversion problems was introduced by Jackson [16].

2.7.1. Bayesian inversion

Bayesian Inversion is an intelligent way of computing a posterior probability by choosing a probability model for the data followed by an assertion of a prior distribution for the unknown model parameters. After the observation of the data, the likelihood function is constructed and the posterior distribution is computed [18].

2.8. Pressure Concepts

The following sections provide a general description of different types of pressure that occur in formations due to geological, chemical and mechanical processes.

2.8.1. Hydrostatic Pressure

Hydrostatic pressure is the total weight exerted per unit area by a static column of fluid above a surface of interest. It is dependent on the height of the fluid column and the fluid density (Mouchet et al., [19] , Figure 2). It is represented by the equation:

$$P_{ho} = \rho g h \,, \qquad (13)$$

In equation (13) fluid density varies according to the type of fluid, concentration of dissolved solids such as salts, other kinds of mineral and/or gases in the fluid column, as well as pressure and temperature conditions at a given depth (Mouchet et al., [19]).

2.8.2. Overburden pressure

Overburden pressure is the total weight exerted per unit area by overlying sediments (rocks and pore fluid) [20]; Mouchet et al., [19] (see figure 2). It is given by the formula

$$S = \int_0^z \rho_b(z)\, dz \,, \qquad (14)$$

where the integral is taken from the sea or ground surface to the depth of interest. If the bulk density is constant then

$$S = \rho_b g z$$

The bulk density is dependent on the matrix density, porosity and fluid density in the pore space. It is expressed as:

$$\rho_b = \phi\rho_f + (1-\phi)\rho_m \,, \qquad (15)$$

The porosity of clay depends on it burial history but generally decreases with depth due to increasing overburden pressure. The relationship between clay porosity and depth can often be approximated by an exponential function. In sandstones and carbonates, the porosity-depth relationship is dependent on many factors such as digenetic effects, sorting and original composition ([20]; Mouchet et al., [19]) (figure 7).

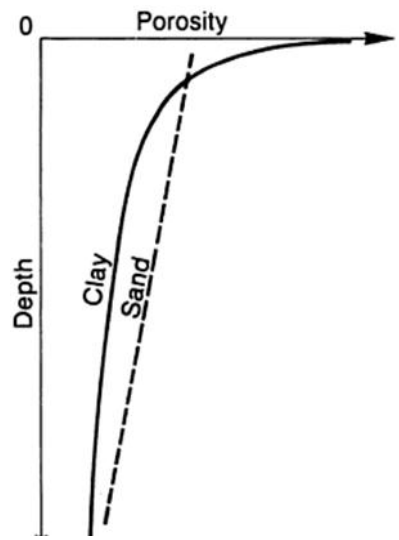

Figure 7. Clay and Sand porosity versus depth profile

2.8.3. Effective pressure

Effective pressure or effective stress is the pressure that acts on the rock matrix. It is defined by Terzaghi as the difference between the overburden pressure and pore pressure. It is one of the key elements that control the compaction of sediments [20]. It is written as:

$$\sigma = S - P, \qquad (16)$$

The method of Bowers [21] relates the vertical effective stress to the velocity by the following expression:

$$v = v_{01} + A\sigma^{B}, \quad (17)$$

The present study uses the following modified form of the Bowers equation which provides a relation between the p-wave impedance and the effective stress:

$$I_p = I_{p0} + \alpha\sigma^{\beta}, \quad (18)$$

The above equation may be inverted for the pore pressure thus:

$$P = S - \left(\frac{I_p - I_{p0}}{\alpha}\right)^{\frac{1}{\beta}}, \quad (19)$$

2.8.4. Pore pressure

Pore pressure or formation pressure is the pressure in the fluid contained in the pore space of rocks (Mouchet et al., [19]; [6]).

- Normal pressure is equal to the hydrostatic pressure of column of formation water extending from the surface to the point of interest. The action of normal pore pressure depends on the concentration of dissolved salts or minerals, fluid type and temperature conditions (Mouchet et al., [19]; [6]).
- Subnormal pressure or a Negative pressure anomaly refers to formation pressure that is less than the hydrostatic pressure at a given location in the subsurface. (Mouchet et al., [19]; [6]) (see figure 8).
- Overpressure or a positive pressure anomaly refers to pressure that exceeds hydrostatic pressure $P_p > P_h$ (Mouchet et al., [19]; [6]) (figure 8).

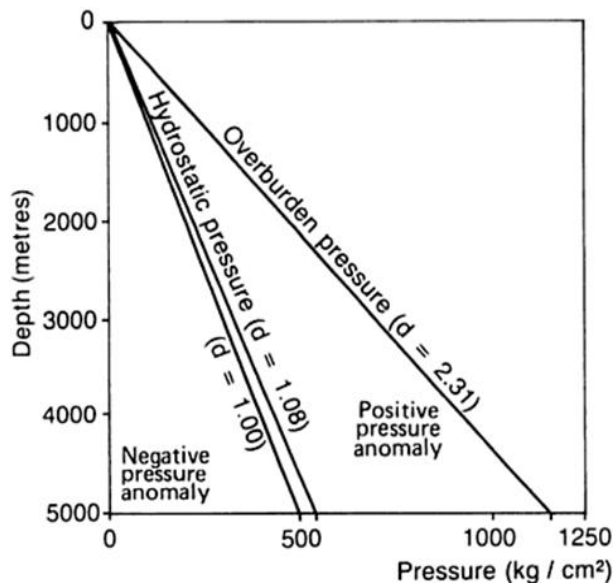

Figure 8. Pressure versus depth relationship Mouchet et al., [19]

2.8.5. Overpressure Origin

This section offers a general description of the causes of overpressure. Overpressure is a phenomenon caused by the movement of fluid due to geological, chemical and mechanical process that occurs in the subsurface of the earth. A partially or completely sealed environment is required for overpressure to develop [20].

Common overpressure mechanisms are described in the following sub-sections:

2.8.5.1. Mechanical compaction process of the sediments or rocks.

Mechanical compaction of sediments occurs during the burial process. Compaction is said to be "normal" if the tendency to compact with increased loading is accommodated without any resistance from the pore fluid. . Under such circumstances the pore fluid is readily expelled and the pore pressure remains normal.. However if the sedimentation rate is fast or the permeability is low, the fluid becomes trapped in the pore space. Compaction is impeded and excess pressure develops in the pore space. This mechanism of overpressuring is known as "disequilibrium compaction" [20]; Mouchet et al., [19].

2.8.5.2. Clay dehydration and/or changes due to burial digenesis

Clay is made of fine sediments with low permeability that varies from 10^{-1} to 10^{-7}mD. The poor interconnection between pores allows fluid to be transferred on a geological time scale. Its ability as a seal depends in its layer thicknesses and capillarity. Smectite or swelling clay is an example of a clay type found in the many basins with water bound in the clay at 150-250 ^{o}F due to dehydration. Smectite is transformed into illite and interlayer bound water is transformed into free pore water, consequently the pore size is enlarged and the pore pressure is increased if the produced free water cannot escape ([20]; Mouchet et al., [19]).

2.9. Drilling Problems Caused by Overpressure [22]

This section presents some of the common problems experienced during the drilling process which are of great concern to scientists and engineers because they can significantly increase the costs of hydrocarbon exploration.

It is often difficult to avoid drilling into geopressured zones because of their high potential to produce hydrocarbons. For example, some shales are good gas producers but their prolific generation of gas leads to an overpressured condition. In deepwater the challenges associated with overpressure are amplified by the high costs of drilling. The following problems are particularly severe in deepwater:

- Small tolerance between the pore pressure and fracture pressure which results in narrow pressure margins while drilling.
- Shallow-water flow hazards caused by pressured aquifer sands.
- Excessive casing programs leading tolost rig time and small holes at total depth.
- High costs due to slow rates of penetration caused by uncertainty over the correct mud weight to use in geopressured zones .

3. Methodology

In this section procedures to predict the pore pressure ahead of a bit are shown. In nutshell, the study involves computing the Fourier transform of a synthetic seismogram recorded at the top of a horizontally layered medium whose layer properties (density, velocity, layer thickness) are known. The synthetic seismogram data is then inverted in the spectral domain for these same layer properties. The inversion is subject to carefully chosen and practical constraints in order to reduce the range of possible solutions. A modified Bowers-type transform is used to convert the inferred acoustic impedance to pore pressure. The results are validated by comparing the inferred layer properties with the actual ones.

The test problem used in this study is based on log data (velocity, density and shale content) acquired from the well Walker Ridge 313-H (WR 313-H) in the Gulf of Mexico. Inversion of the synthetic seismogram data was accomplished using a Bayesian method which evaluates the posterior probability of the inferred parameters given the measured data and prior constraints.

A method due to Ganley [15] was used to generate the Fourier transform of the synthetic seismogram. This method requires the low-frequency phase velocities of sedimentary layers. The sonic velocities acquired from WR 313-H were assumed to be equal to the phase velocities of the sediment at 100 Hz and then converted to low-frequency phase velocities using eqn (10). This was a formality. The correct conversion is not known and immaterial to the objective of the study which was to demonstrate that for a given set of low-frequency velocities, however obtained, it is possible to infer these velocities (or associated impedances) using synthetic seismic data generated from them.

The bulk densities in WR 313-H were used without additional processing except for upscaling. This aspect will be discussed in Section 3.1.1. The sonic log data from WR 313-H is represented by the black curve in (figure 9a), and density in green in Figure 9b.

Sonic velocity

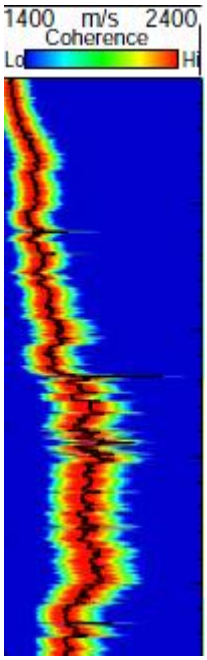

a)

Density

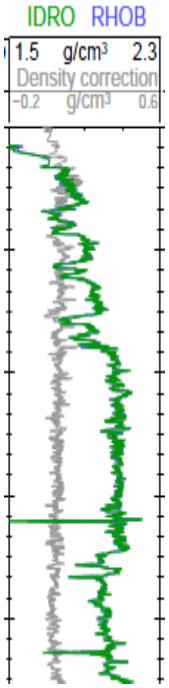

b)

Figure 9. (a, b) Velocity and density log extracted from [3];

3.1. Synthetic data example.

In the following sections the generation of synthetic data used for the inversion procedure is described.

3.1.1. Generation of sedimentary Column from log data of Walker Ridge 313-H (WR 313-H).

Shale fraction logs from WR 313-Hwere used to construct a binary-layer sedimentary column consisting of sands and shales. The procedure was as follows:

- A thicker column was constructed by scaling all depths by a factor of 3.28.
- A sand-shale index was defined from the volume of shale assuming a cut-off value of 0.4.
- Using this index, another index was constructed to represent positions in the log at which interfaces between sand and shale were located..
- The depths corresponding to these interfaces were identified and the thicknesses of individual sand and shale units were calculated.
- Depths at the mid-points of layers were computed.

The resulting column contained alternating sand and shale layers of varying thickness (figure 10).

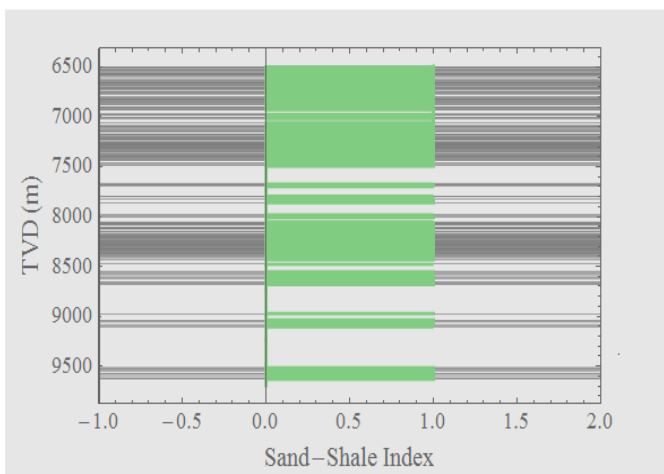

Figure 10. Sand-shale index.

Log densities and velocities were upscaled to the resolution of these layers. Density upscaling was done using volumetric averaging whereas velocity upscaling was carried out using Backus-Gilbert averaging.

3.1.2. Generation of histograms for Layer Thickness

The problem of inverting zero-offset seismic data for velocity or density ahead of the bit is fundamentally ill-posed. However the solution can constrained by imposing "soft" statistical constraints on the thicknesses of individual layers. The underlying premise is that layer thicknesses are not random but obey statistical laws governed by the deposition process. This section describes how layer thicknesses are characterized statistically. The study investigated single-variate and the bivariate probability distributions for the thicknesses of layers in the column described in Section 3.1.1. In order to capture spatial correlation between layers, bivariate probability density functions characterizing the joint probability of the thicknesses of two neighboring layers were considered (figure 11).

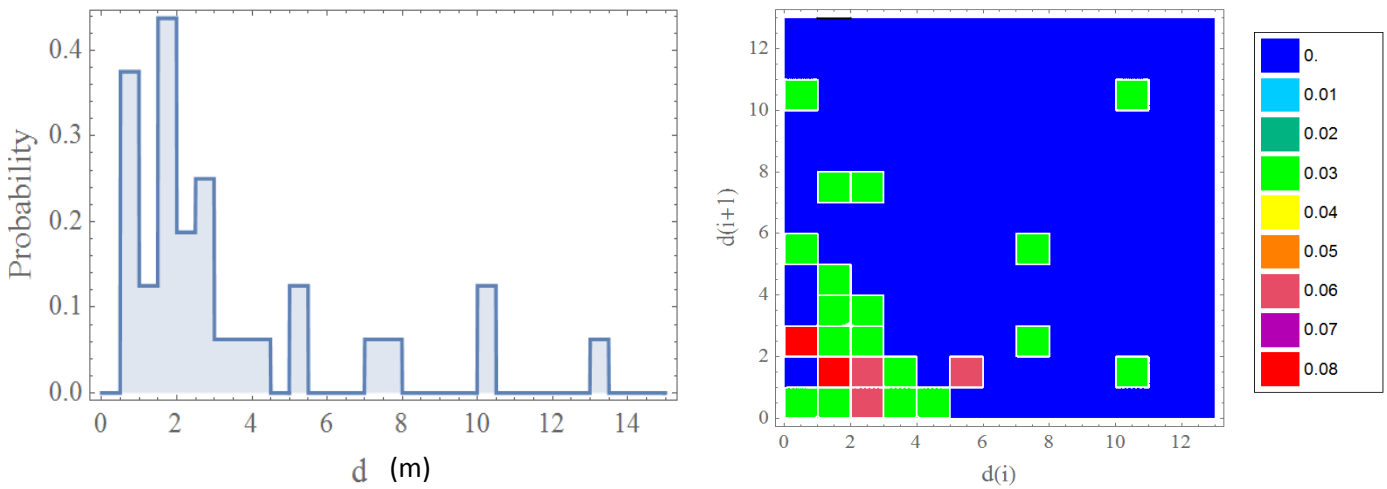

a) b)

Figure 11. a) Histogram of layer thicknesses; b) Joint histogram of neighboring layer thicknesses .

Parametric and non-parametric probability distributions were used to model the histograms shown in (figure 11). Uni-variante and bi-variate exponential distribution functions were chosen as suitable parametric models. This choice was based partly on the work of Mukhopadhyay et al [24] who analyzed the thicknesses of 250 layers of Cove turbidity sediments. They found these thicknesses obeyed an exponential distribution with a mean of 1.04 m.

(Figure 12) shows the goodness of fit between the histogram probabilities (figure 11a) and the probabilities generated by fitting a uni-variate exponential distribution to this data. The fit is not very good with very few data points falling on the line representing perfect agreement between the two sets of data.

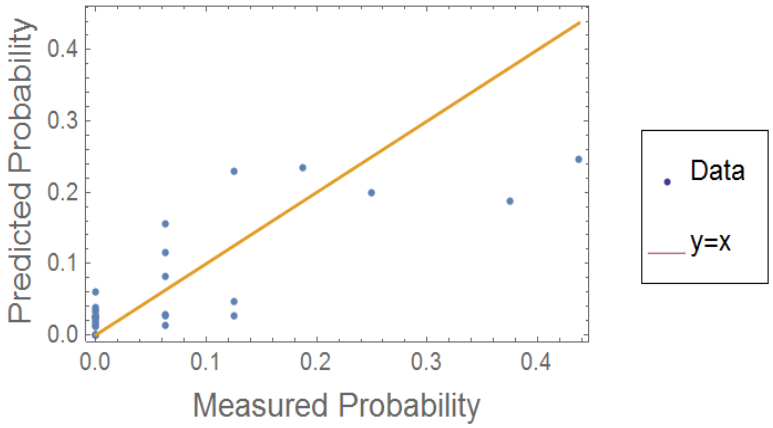

Figure 12. Predicted versus measured probability of layer thicknesses for single variate order.

There are several bi-variate distributions in the literature Kotz et al [23]. The Freund bi-variate exponential distribution was chosen for this study. (Figure 13) shows the goodness of fit to the bi-variate histogram data shown in Figure 11b. The fit is inferior to that obtained using the uni-variate exponential model (Figure 12). .

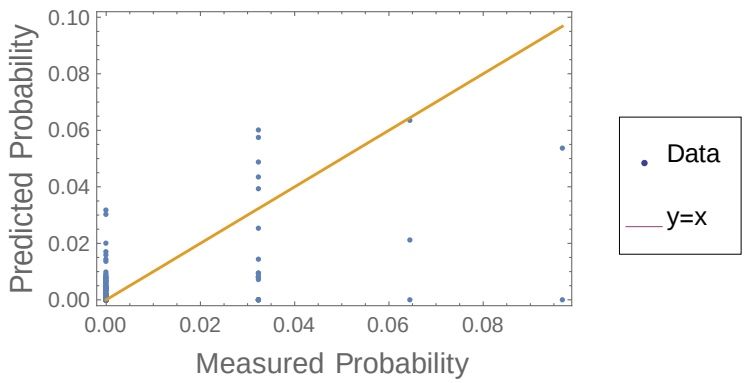

Figure 13. Predicted versus measured probability of layer thicknesses bivariate order.

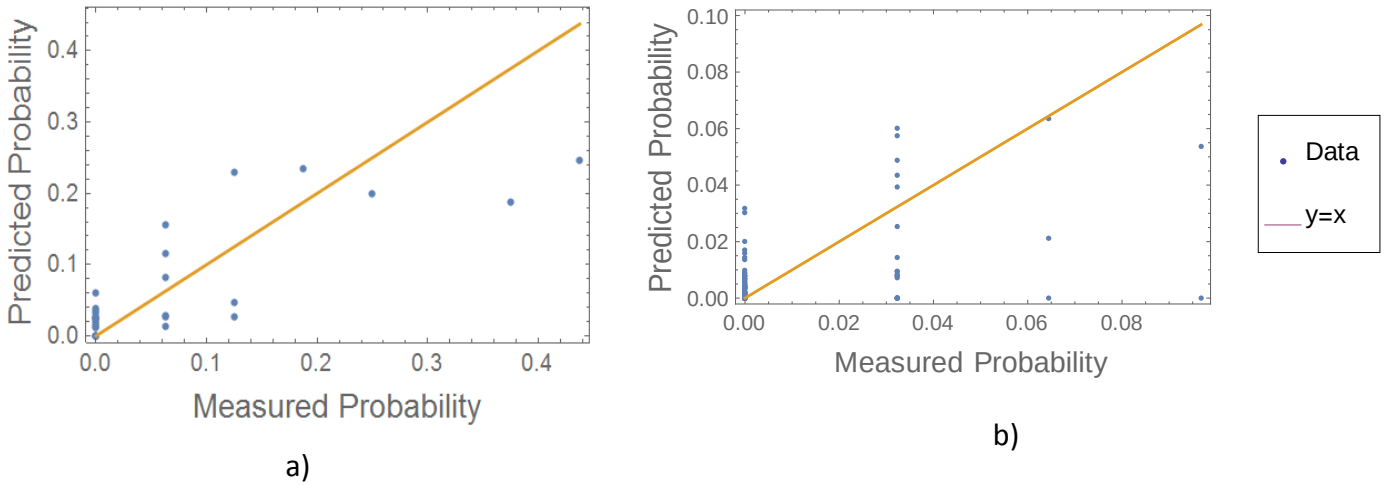

Figure 14. a) Predicted versus measured probabilities of layer thickness for the uni-variate case.; b) Predicted versus measured probabilities of layer thicknesses for the bi-variate case.

After generating histograms , velocities and densities were upscaled from log-scale to the resolution of the layers. The fine-scale and upscaled velocities are plotted a functions of depth in Figure 17. An apparent misfit between the upscaled and fine-scale velocities occurs from 7500 to 7700 m, 8650 to 8950 m, and from 9250 to 9550 m indicated by the arrows. However closer inspection shows that this feature is an artifact of distant points in the upscaled log being joined together by straight lines (figure 15).

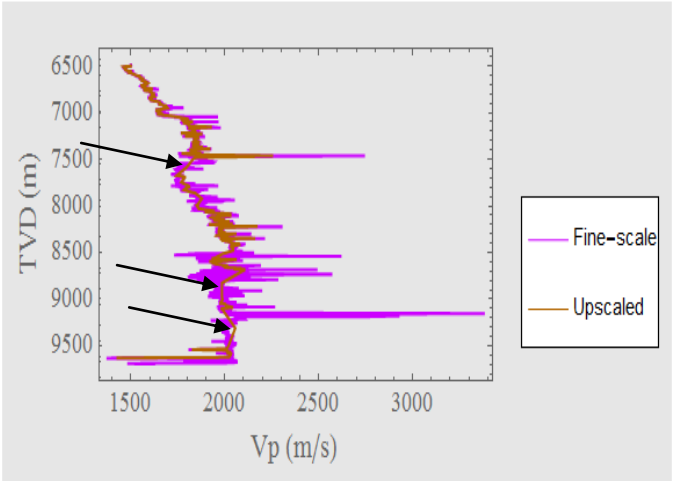

Figure 15. Fine-scale and upscaled velocities versus depth

The seeming mismatch described above for velocities was also observed for density at the same depth intervals (figure 16).

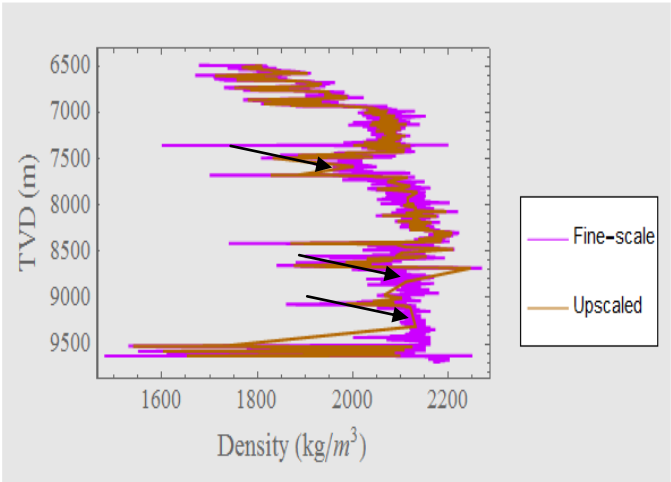

Figure 16. Fine-scale and upscaled densities versus depth

3.1.3. Synthetic Seismogram

VSP tools provide seismic data useful for inferring the properties of the earth. Before examining inversion consider first the forward problem of generating a synthetic seismogram from known rock properties table 1. For a three-layer model, an impulsive seismic source was fired and the resulting zero-offset seismogram at the surface was computed using the method of Ganley[15]. The Fourier transform of the signal recorded at the surface is represented by eqn (6). The seismogram is symmetrical and the energy of peak amplitude ranges from 0 to 250 frequencies (figure 17).

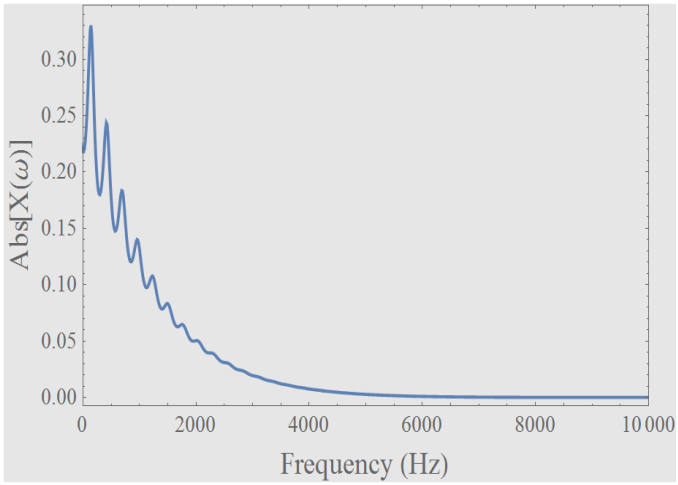

a)

Figure 17. Spectral representation of the synthetic seismogram generated by an impulsive source fired at the top of a 3-layer model.

The inverse Fourier transform of the synthetic seismogram for 3 layers was computed yielding the time domain representation of the synthetic seismogram in (figure 18) where the yellow dot represents the layers interfaces.

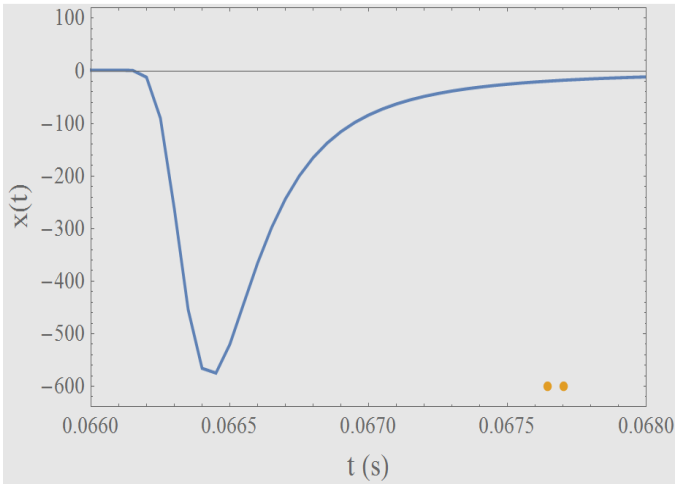

b)

Figure 18. Time domain representation of the synthetic seismogram produced by an impulsive source fired at the top of a 3-layer model.

The seismogram in figure 17 was generated by an impulsive source. A more realistic source can be represented by a Ricker wavelet. A Ricker wavelet [15] with a peak frequency of 50 Hz was chosen as the source wavelet (figure 19).

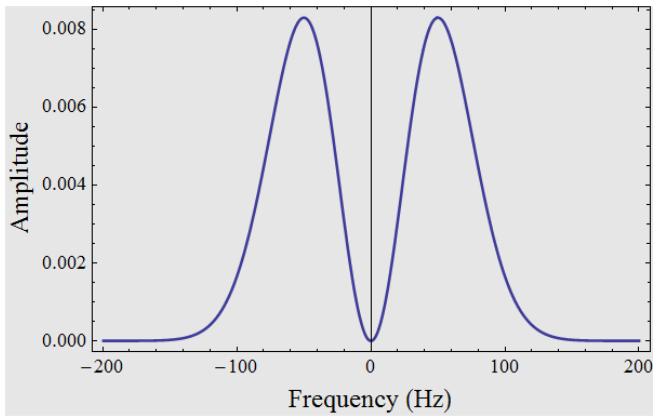

Figure 19. Frequency domain representation of a Ricker wavelet.

Convolution of the Ricker wavelet with the synthetic seismogram produced by an impulsive source gives the synthetic seismogram produced by a Ricker wavelet source. The same result can be achieved via multiplication in the frequency domain. (Figure 20) shows the product of the Fourier transform of the Ricker wavelet and that of a synthetic seismogram produced by an impulsive source.

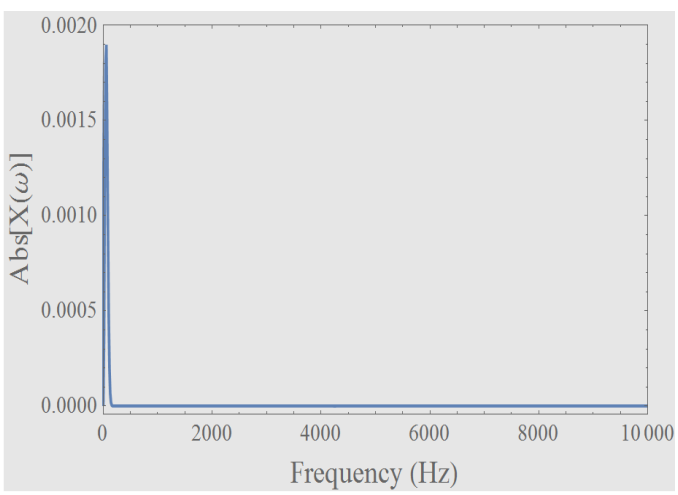

Figure 20. Synthetic seismogram from Ricker wavelet source in frequency domain.

The inverse Fourier Transform of this product gave a smoothed time-domain representation when compared with the synthetic seismogram produced by an impulsive source (figure 21).

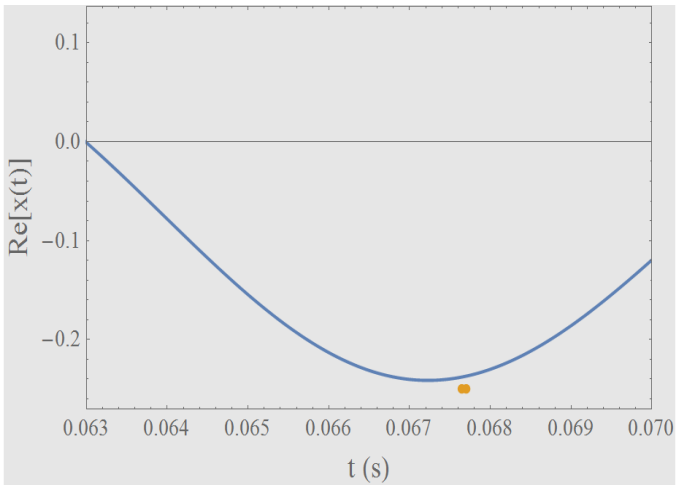

Figure 21. Synthetic seismogram from Ricker wavelet source in time domain.

3.1.4. Synthetic Seismogram example for 32 Layers

In order to make the problem computationally feasible, the sedimentary column was truncated to a height of 100 m. This subset of the original column consisted of 32 sand and shale layers. In order to solve the governing equations, a boundary condition prohibiting transmission of upward going waves through the base of the column was imposed. This was equivalent to giving the bottom layer an infinite thickness. (Figure 22) shows the Fourier transform of the seismogram produced by an impulsive seismic source fired at the top of the 32-layer column. It is interesting to note the synthetic seismogram shows significant energy at relatively high frequencies beyond 2000 Hz.

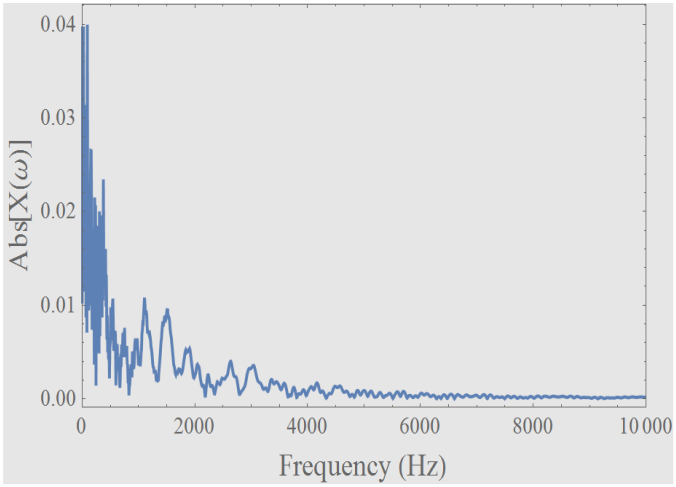

Figure 22. Spectral representation of synthetic seismogram generated by an impulsive source

Taking the inverse Fourier transform gave the corresponding waveform in the time domain (figure 23).

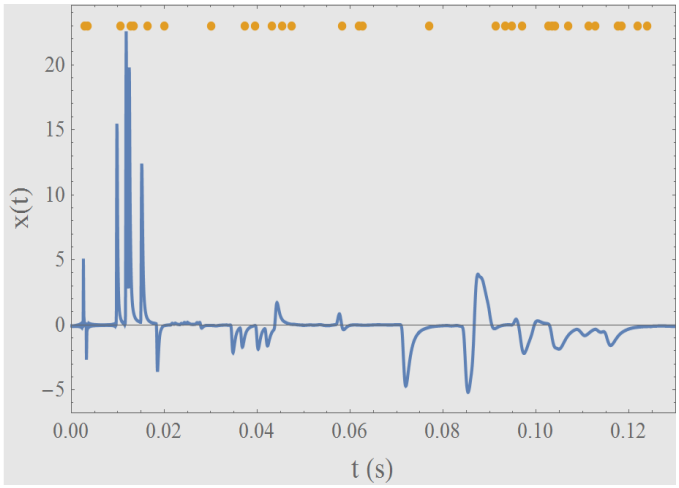

Figure 23. Synthetic seismogram produced by impulsive source in the time domain. Yellow dots represent the approximate two-way travel times of the two shallowest layer boundaries computed using phase velocities at zero frequency.

To get a synthetic seismogram produced by a typical source wavelet, it was necessary to use the Ricker wavelet as was done for the 3-layer case. To achieve this step the synthetic seismogram generated by an impulsive source (figure 22) was convolved with the wavelet of the input signal in time domain. Equivalently the seismogram and input wavelet were multiplied in the frequency domain yielding the synthetic seismogram from a source wavelet (figure 24).

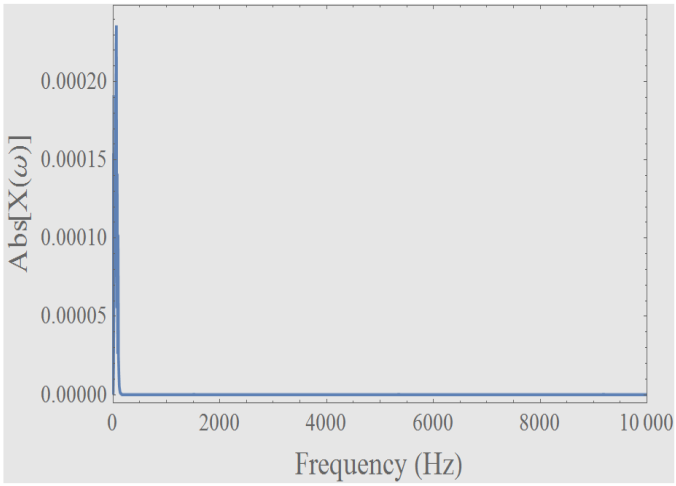

Figure 24. Fourier transform of synthetic seismogram generated by a Ricker wavelet source

Taking the inverse Fourier Transform of the synthetic seismogram of (figure 24) produces the following smoothed response compared with (figure 25).

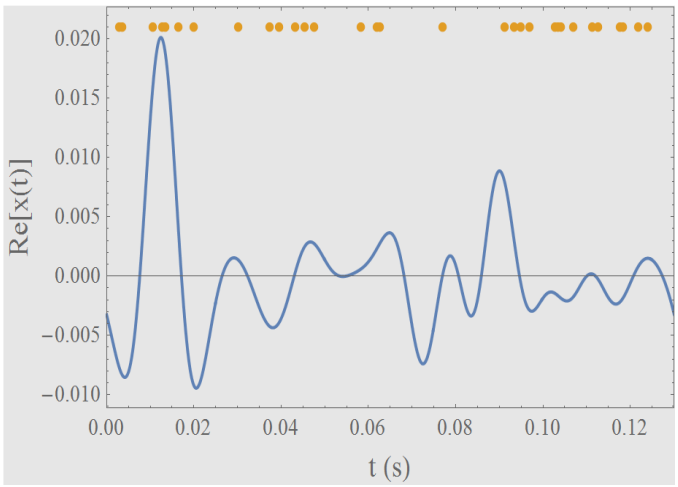

Figure 25. Synthetic seismogram produced by a Ricker wavelet. Yellow dots represent the approximate two-way travel times of the two shallowest layer boundaries computed using phase velocities at zero frequency.

3.2. Methodology used for Monte Carlo Inversion

In Section 3.1.4, the Fourier transform of the synthetic seismogram generated by firing a Ricker wavelet source at the top of a 32 layer medium was computed. In this section the methodology used to address the corresponding inverse problem is described. The purpose of the inversion is to invert the Fourier transform of the synthetic seismogram generated in Section 3.1.4. for the velocities, densities, and thicknesses of all 32 layers. A prior constraint on the inversion is that the layer thicknesses are distributed according to a non-parametric distribution function with known parameters. Upper and lower bounds for the velocities and densities in clays and sands are also known. Note that the Q-factor that controls absorption was not inverted. The Q-factor is assumed to be known and uniformly equal to 60. Inversion of the Q-factor can be explored in future studies.

After trial and error, it was determined that further constraints would be needed in order to obtain satisfactory results. It was assumed that the velocity and density were known up to a specified distance below the top of the layer. The points at which velocity and density are known below the seismic receiver are referred to as “anchor points”. Such anchor points could in practice be obtained by placing sonic and density tools below the borehole seismic tool. The objective of the inversion described in this section is to infer the velocity and density profiles below the deepest anchor point.

At the start of the inversion, initial guesses consistent with prior knowledge are generated for the layer thicknesses, densities, and velocities. These guesses represent the initial position of the random walker. In order to draw samples from the posterior probability distribution, the random walker moves from one position to another in model space following the rules of the Metropolis algorithm. Specifically, the likelihood function which measures the distance between the measured and the computed seismogram was determined. Multiplication of the likelihood function with a priori probability density function yields the posterior probability of model parameters. A new proposed position of the random walker is either retained or rejected depending on how the value of the corresponding posterior probability compares with the posterior probability of the previous position. In the limit as the random walker visits a large

number of sites, the collection of retained models converges to an ensemble drawn from the posterior distribution.

The initial guesses for the layer thicknesses are drawn from an exponential distribution with an average layer thickness that is similar to the actual average layer thickness. A histogram of the initial guesses for the layer thicknesses is shown in fig 26a. It shows a consistent decrease of probability with layer thicknesses while for the actual (or "true") model the variation is not as consistent (fig. 26b).

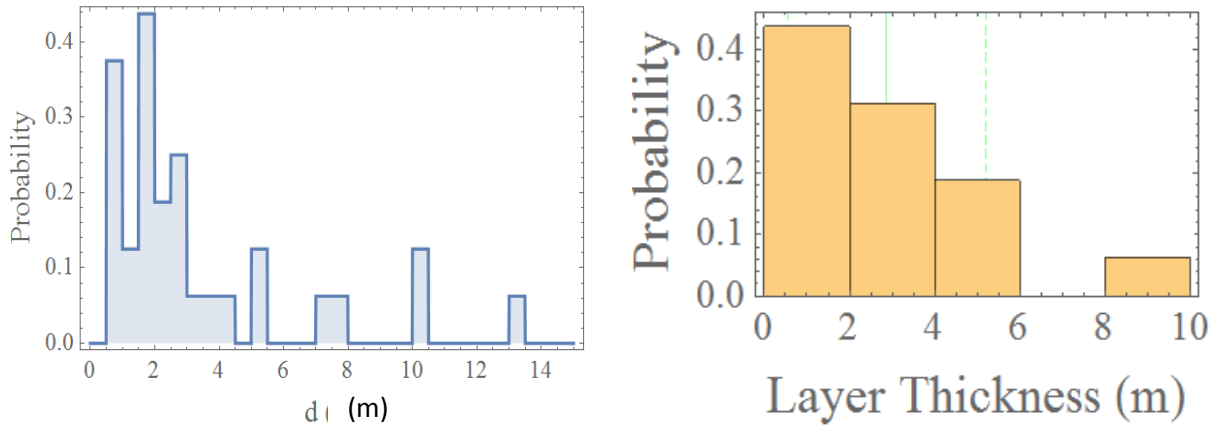

a) b)

Fig 26. (a) Histogram of initial layer thicknesses; (b) Histogram of actual layer thicknesses

The layer velocities of the initial model were drawn from two boxcar distributions, one for sands and another for clays. Two sets of velocity profiles were generated, one for each lithology. The actual profile was constructed by alternatively picking points in depth from these two sets of profiles. The resulting values are shown in figure 27a. A similar scheme was adopted to construct the density profile (figure 27b).

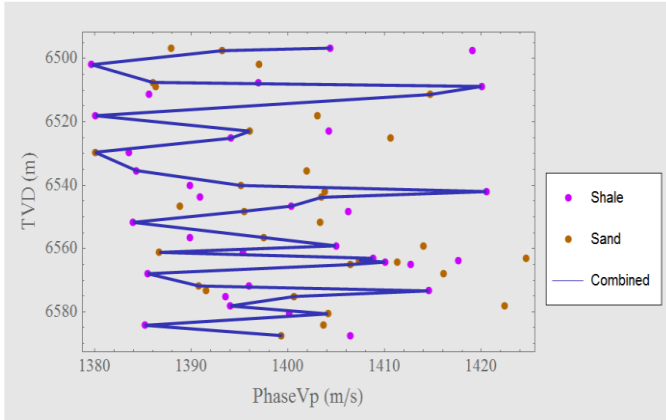

a)

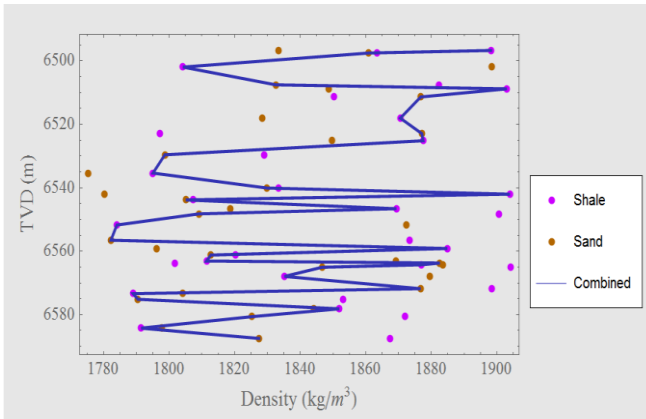

b)

Figure 27. Initial sand velocity (a), and density (b). Purple dots are shale points. Brown dots are sand point. Blue curves show final profiles picked from sand and shale points.

(Figure 28) shows a comparison between the initial and actual velocity and density profiles. The actual velocity values ranges between 1815 and 2470 m/s and the initial velocity between 1950 and 2650 m/s. The density ranges from 1740 to 2120 Kg/m^3 for the actual model and from 1700 to 2140 Kg/m^3 for initial guess.

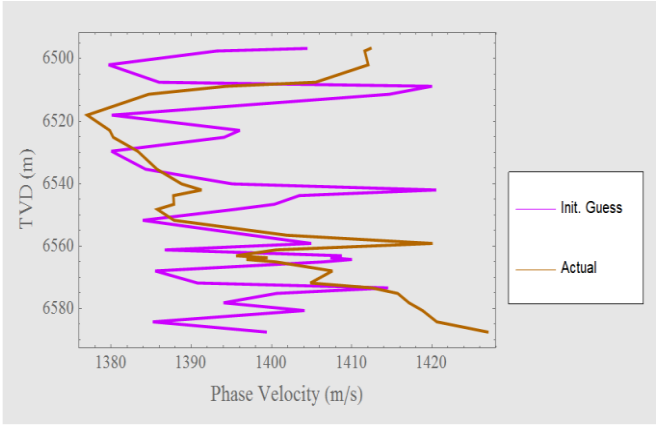

a)

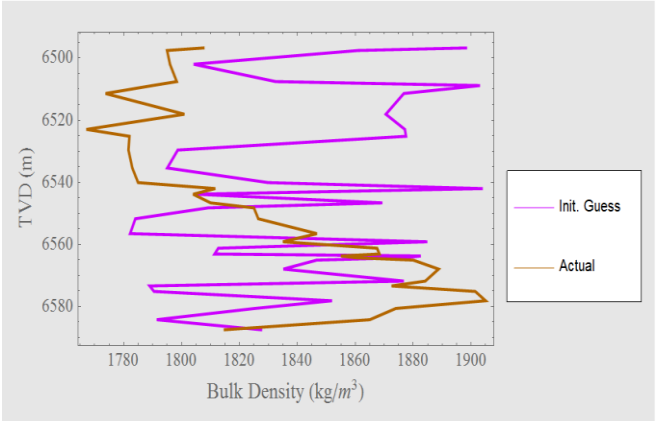

b)

Figure 28. (a) Actual (brown) and initial (purple) phase velocity profiles (b) Actual (brown) and initial (purple) bulk density profiles.

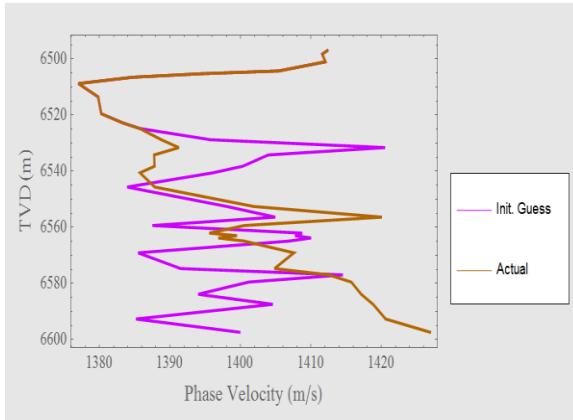

a)

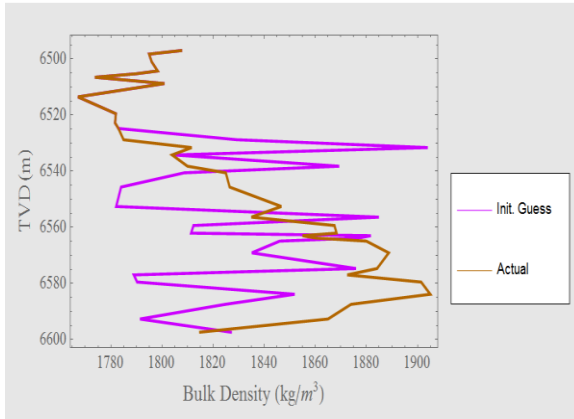

b)

Figure 29. (a) Actual (brown) and initial (purple) phase velocity profiles (b) Actual (brown) and initial (purple) bulk density profiles.

The synthetic seismogram for the initial model was computed and compared with the actual synthetic seismogram (fig 30). The real parts of both seismograms are symmetrical about the vertical axis (figure 30a) whereas the imaginary parts are anti-symmetrical about the same axis (figure 30b). This is a feature of spectrums of real-valued functions.

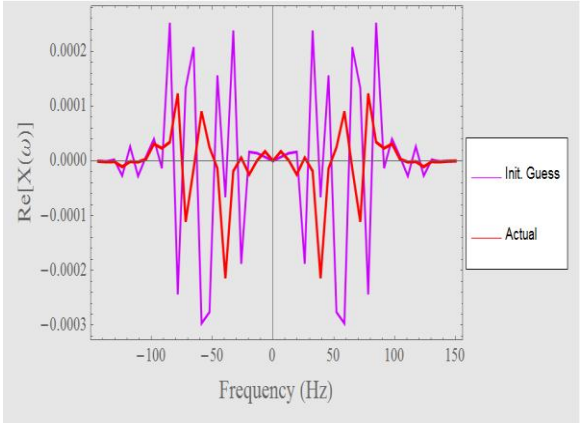

a)

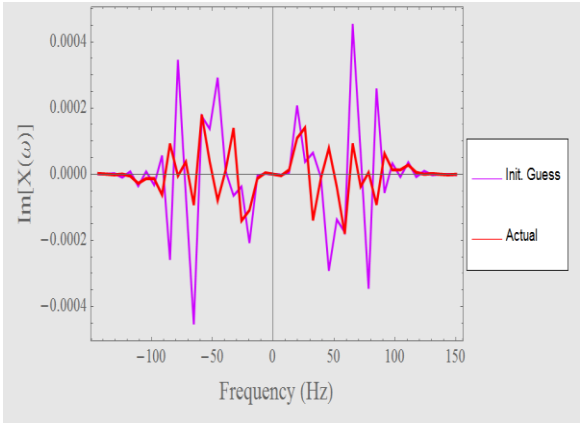

b)

Fig 30. Fourier transform of synthetic seismogram corresponding to initial (purple) and actual (red) models. (a) Real part. (b) Imaginary part.

4. Result

This section describes the results obtained by running the inversion code, written in Mathematica®, to generate samples from the posterior probability density function (PDF).

During the simulations between 1 million and 10 million samples were drawn from the posterior PDF. The progress of the simulations was observed by measuring the scalar distance between two vectors representing the actual property profile and the current position of the random walker. Figure 33 shows the scalar distance measure for the phase velocity over the course of 1milion iterations. It is interesting to note that the distance between the two vectors is larger after 1 million iterations than at the beginning which means the inversion did not make any improvement over the initial guess (figure 31).

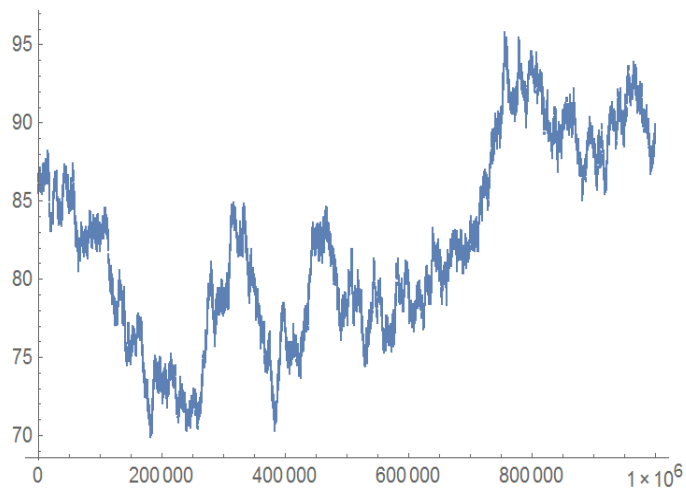

Figure 31. Phase velocity difference versus iteration number

(Figure 32) shows a similar plot for the density. Unlike the phase velocity, a significant decrease in the density difference relative to the initial guess is apparent after 1milion iterations. The density difference plot presents similar behavior shown in the phase velocity curve. It is also evident that no improvement was attained in the initial model of density for 10million samples.

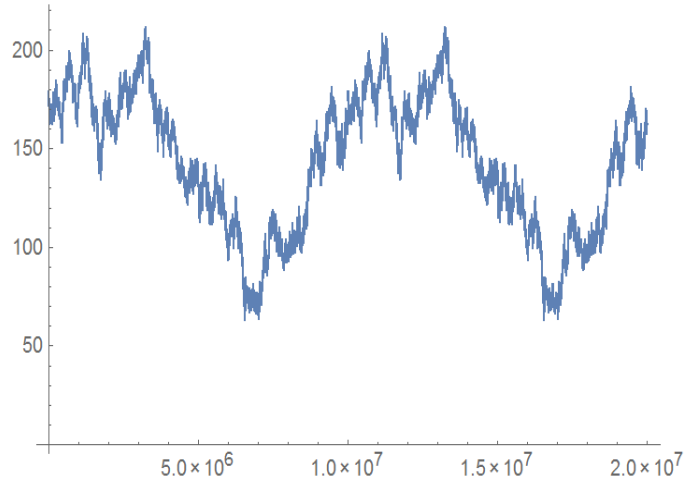

Figure 32. Bulk Density difference versus iteration number.

The total depth of the sedimentary column at each position of the random walker in the model space is shown in the figure 33.

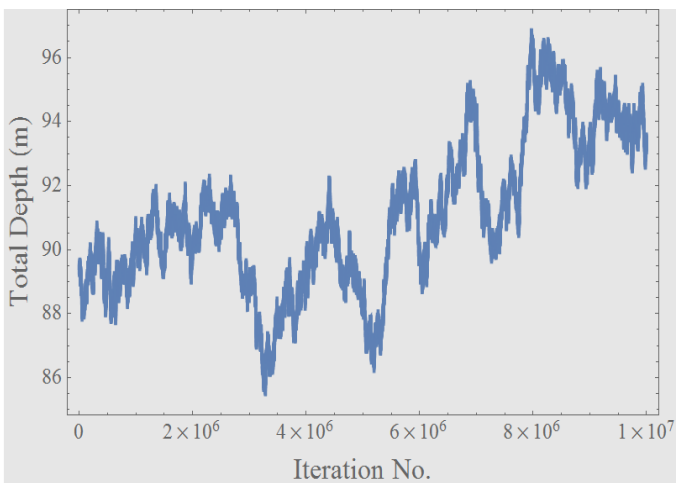

.

Figure 33.Column height versus iteration number.

The posterior PDF is plotted versus iteration number in (figure 34). The band of points situated between $10^{-70}$and 10^{-85}after 200,000 iterations suggests no improvement over the initial guess.

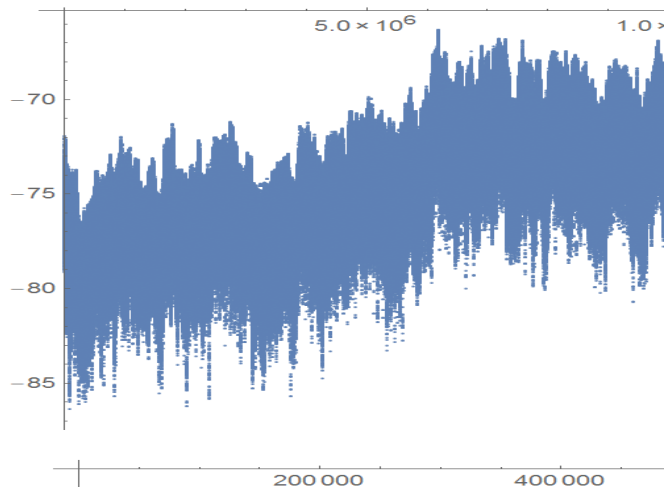

Figure 34. Logarithm of the posterior probability density functions versus iteration number.

In (Figure 35), the synthetic seismogram corresponding to the maximum likelihood result after 1 million iterations is compared with the actual synthetic seismogram. Both the real and imaginary parts agree almost perfectly. The metropolis algorithm is able to find many different combinations of layer properties that produce the same seismogram as the actual sedimentary column.

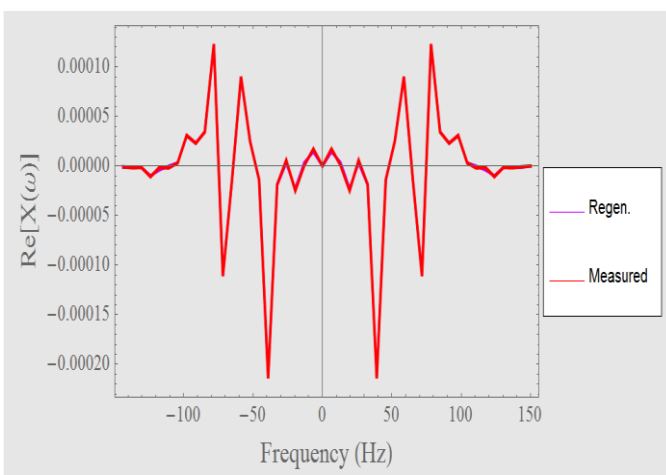

a)

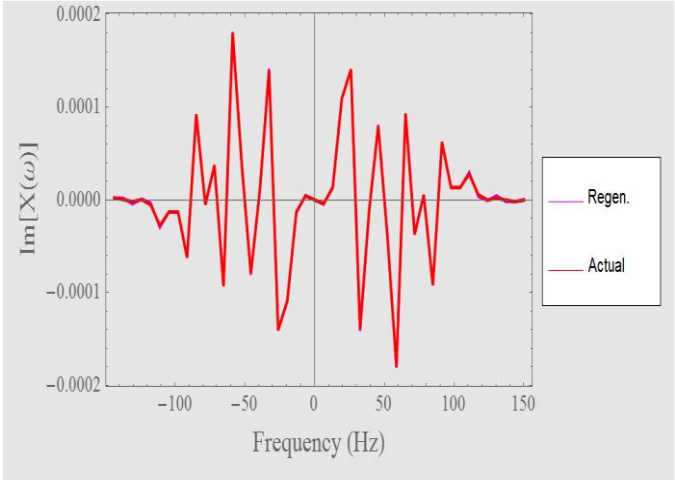

b)

Figure 35. Comparison of true synthetic seismogram (red) with that regenerated from maximum likelihood solution (purple). (a) Real part; (b) Imaginary part.

The (figure 36) shows the profiles of layer thickness as functions of layer number. It can be observed that actual layer thicknesses frequently fall outside the 80% confidence interval bounded by the P10, and P90 probabilities (figure 36a). In figure 36b) the 50% percent probability (P50) and the initial model are slightly shifted but the maximum likelihood compares better with the actual profile which indicate that the median (P50) and maximum likelihood profiles show little improvement when compared with initial profile.

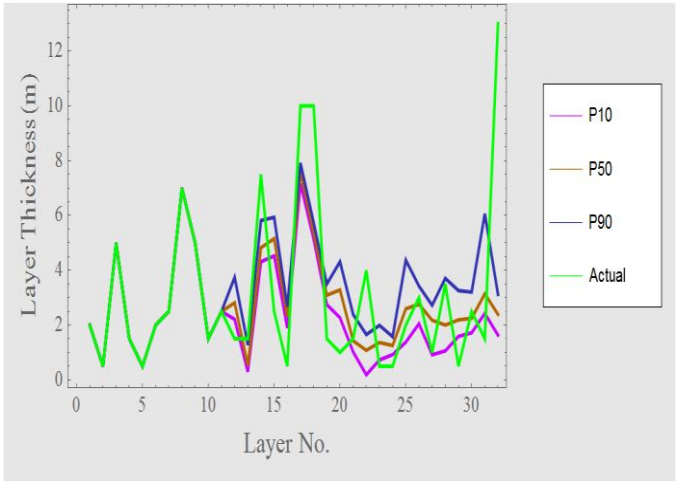

a)

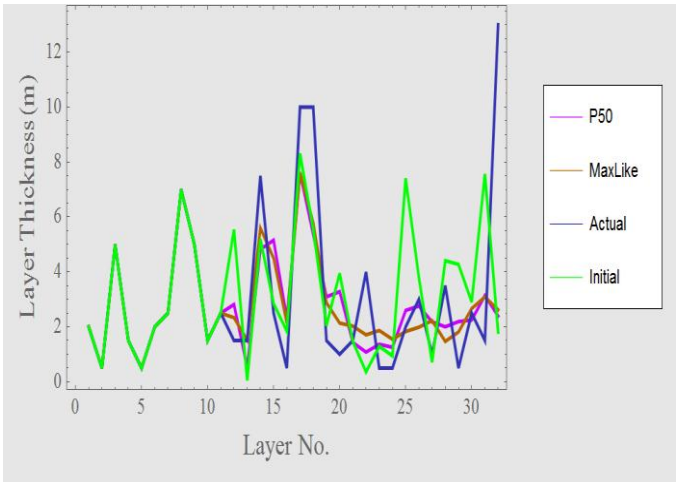

b)

Figure 36a). P10 (purple), P50 (brown), P90 (blue), and actual (green) layer thicknesses versus layer number.

Figure 36b). Median (purple), maximum likelihood (brown), initial (green) and actual (blue) profiles of layer thicknesses versus layer number

In the (figure 37) is shown the P10, P50, P90 and actual phase velocity profiles versus the layer number.. The range of phase velocities between the P10 and P90 estimates encapsulated actual velocity profile very well. However the agreement between the P50 and the actual velocity profiles is poor.

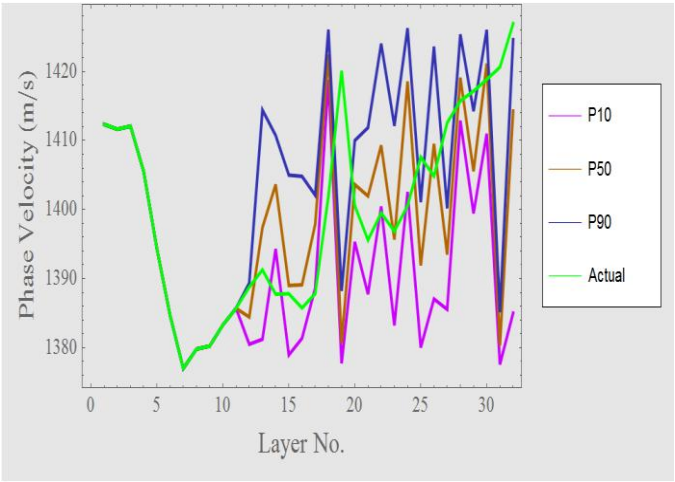

Figure 37. P10 (purple), P50 (brown), P90 (blue) and actual (green) profiles of phase velocities.

Plots of the P50, maximum likelihood, actual and initial phase velocities are shown in (figure 38) The P50 and maximum likelihood results follow the trend of the actual phase velocity profile but they exhibit considerable noise.

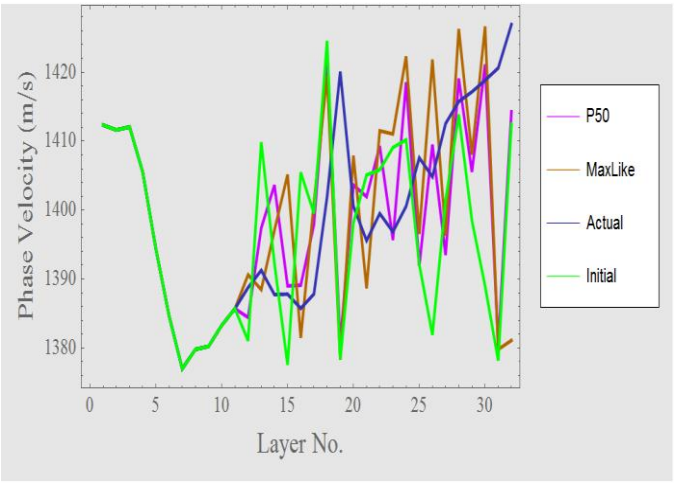

Figure 38. Median P50 (purple), maximum likelihood (yellow), initial (green) and actual (blue) profiles of phase velocities.

The maximum likelihood, actual and initial models are plotted versus depth in the (figure 39). These curves have been upscaled to a resolution 15 m, typical of a VSP measurement. It is visible that the fit among the velocity profiles is not bad. The maximum likelihood and the initial model show approximation with actual profile from 20m to 50m depth but they shift from

actual direction below 50m depth. The agreement observed is a sign that the inversion process improves the initial model.

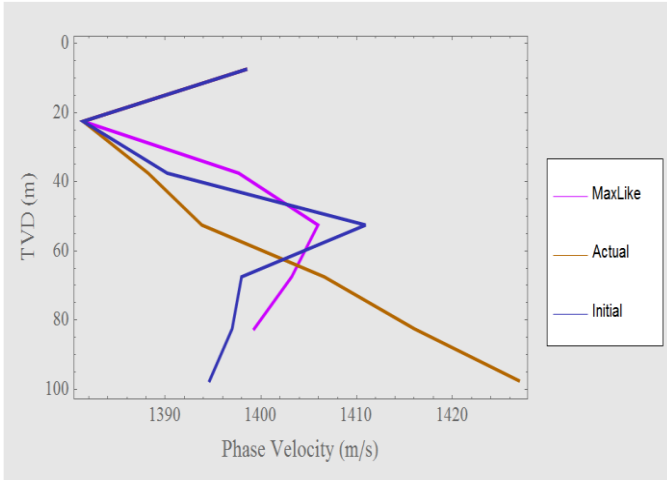

Figure 39. Maximum likelihood (purple), initial (blue) and actual (yellow) profiles of phase velocities

The P10, P50, P90, and actual density profiles are shown in the (figure 40). The actual density is not constrained by the P10 and P90 estimates and shows poor agreement with the P50 profile.

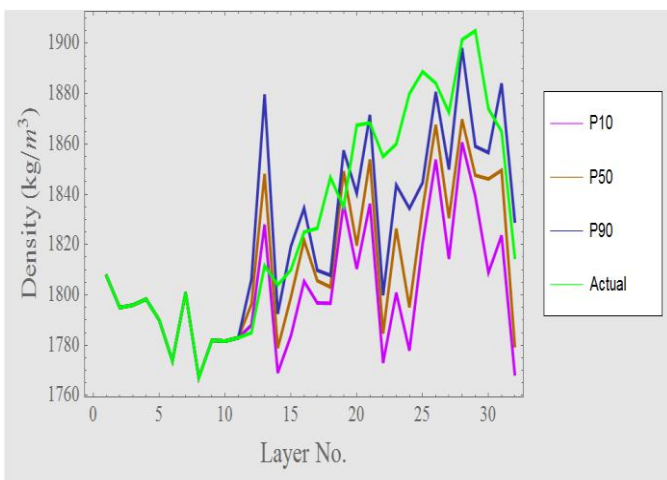

Figure 40. P10 (purple), P50 (yellow), P90 (blue) and actual density profiles

In the (figure 41) are shown the P50, maximum likelihood and initial densities along with actual density profile.

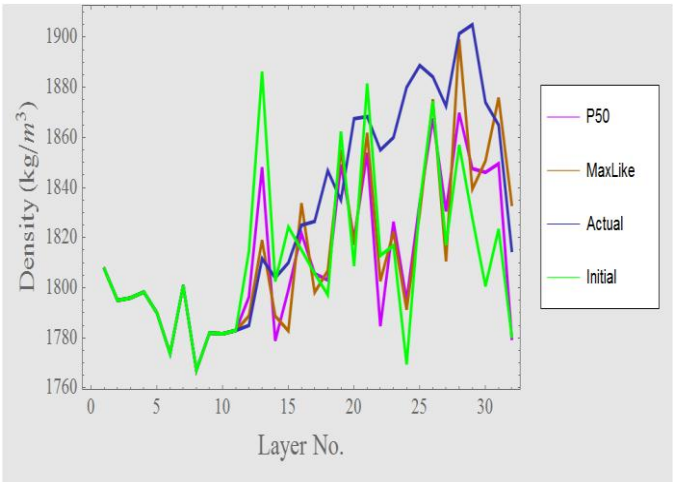

Figure 41. Median P50 (purple), maximum likelihood (brown), initial (green) and actual (blue) density profiles.

The plots in (figure 42) show the maximum, initial and actual density profiles upscaled to a 15 m resolution. The fit is poor. As for the actual profile, the maximum likelihood profile increases monotonically to a depth of 80 m. However this is the only similarity that could be observed between the two profiled.

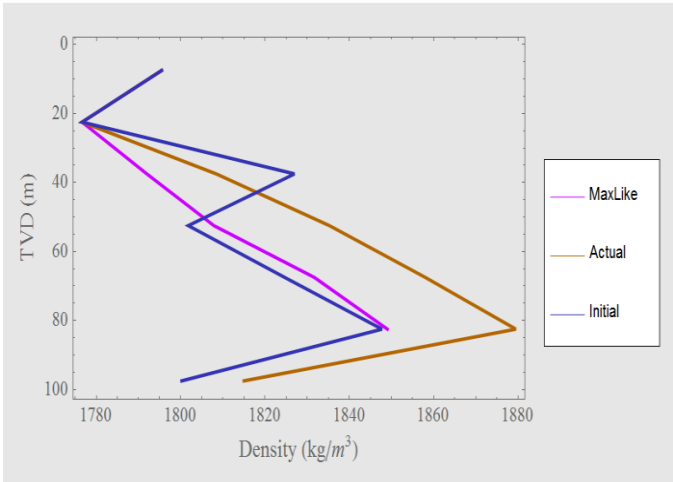

Figure 42. Maximum likelihood (purple), initial (blue) and actual (yellow) density profiles

It is shown the 10%, 50%, 90% probability (P10, P50, P90) and the actual impedance profiles. As in the previous case the upscale was performed in 15 m grid using Backus averaging. Similarly to density profiles the actual impedance is better approximated to (P 90%) profile (figure 43).

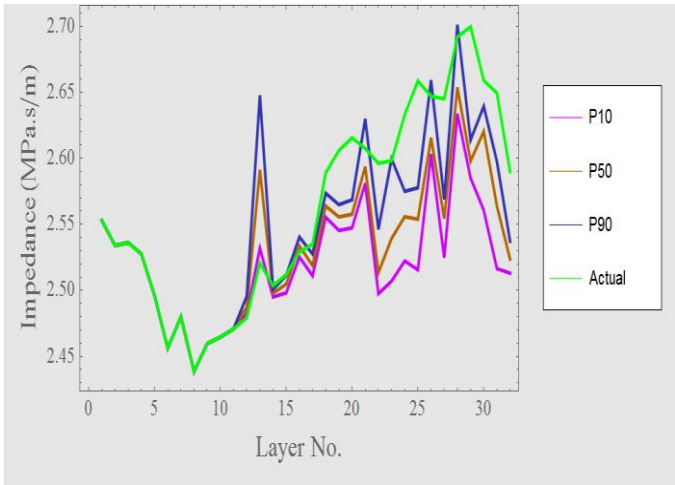

Figure 43. P10 (purple), P50 (yellow), P90 (blue) and actual impedance profiles.

The P50, maximum likelihood and initial upscaled impedances along with actual impedance profile are seen in the figure 50. In the same way they are upscaled to a 15 m grid using volumetric averaging. It is also possible to see that the actual impedance profile is close to P50, maximum, likelihood and initial impedance profile (figure 44).

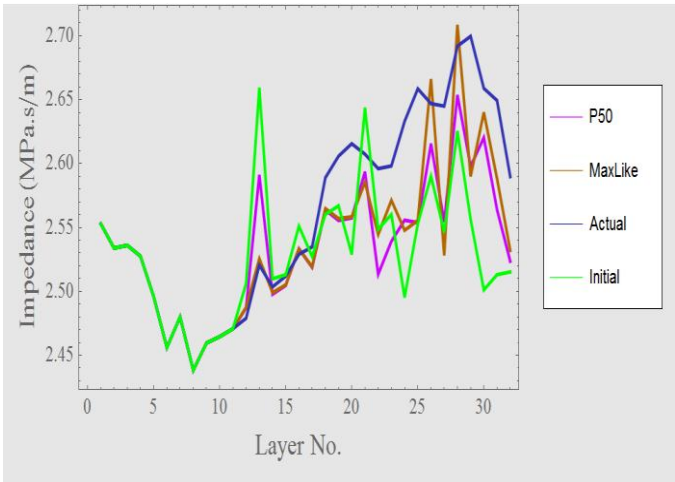

Figure 44. Median P50 (purple), maximum likelihood (yellow), initial (green) and actual (blue) impedance profiles.

The (figure 45) shows the maximum, initial and the actual impedance profiles. Although the initial model is slightly shifted from the actual to maximum likelihood profile, no doubt the fit among the curves is good and the inversion improved the initial impedance profile compared to the density. It is relevant to notice how better the maximum likelihood impedance profile moves closer to actual impedance profile showing a nice impedance profile prediction.

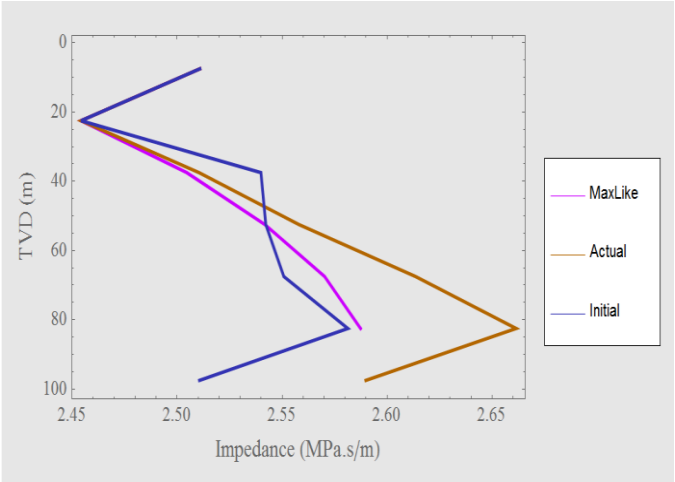

Figure 45. Maximum likelihood (purple), initial (blue) and actual (yellow) impedance profiles.

In the impedance versus depth plot show similar features described for depth as function of impedance see (figure 46) the second pick in the initial profile coincide with the slight shift observed in the depth versus impedance which also show better maximum likelihood approximation to the actual impedance profiles.

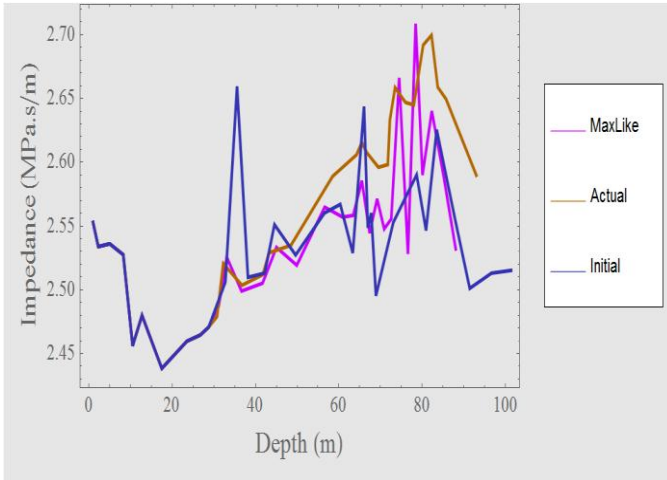

Figure 46. Maximum likelihood (purple), initial (blue) and actual (yellow) impedance profiles versus depth.

Finely the pore pressure is plotted versus depth as can be seen in the (figure 47). It provides with much more visibility a detailed view of the fit between the maximum likelihood and actual impedance profile. The plot also shows a little smooth on the initial pore pressure profile where the initial impedance profile shows a pick.

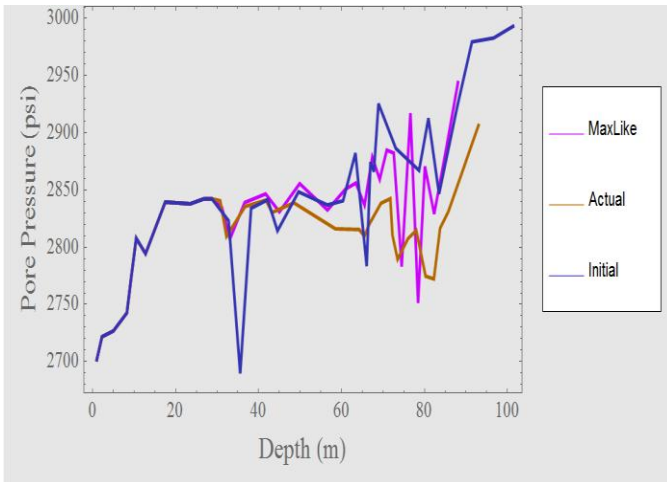

Figure 47. Median P50 (purple), maximum likelihood (yellow), initial (green) and actual (blue) pore pressure profiles.

In the (figure 48) the actual Fourier transform of surface seismogram in red color is shown overlaying the final seismogram in pink. Again no improvement on the fit was attained after 10milion iterations.

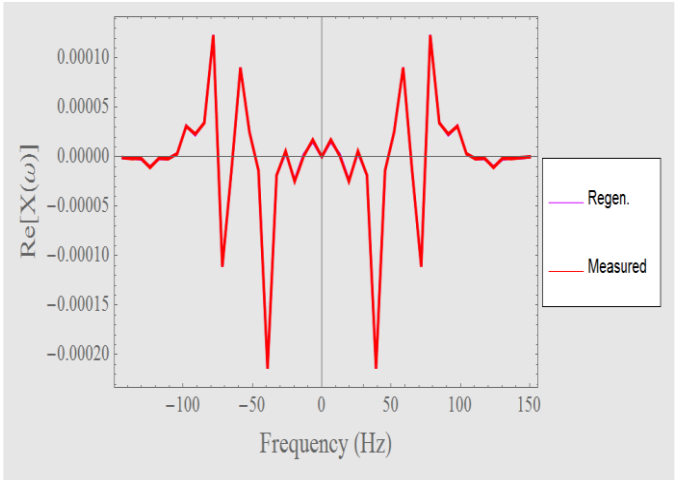

a)

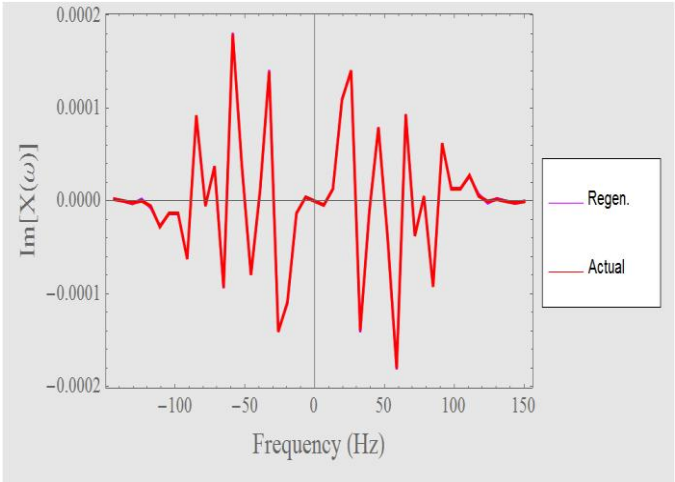

b)

Figure 48. Synthetic seismogram (a) Real part of regenerated synthetic seismogram (in dark purple) and actual synthetic seismogram (in red); (b) Imaginary part of regenerated synthetic seismogram (in dark purple) and actual synthetic seismogram (in red).

The smoothed profiles of 10%, 50% and the 90% percent probability of layer thickness plotted versus iterations number for 10milion samples differ slightly from 1milion (figure 49 a). The approximation of (P10), (P50) and (P90) with actual profile is not good and the misfit also occurs between the maximum likelihood and the actual profile (figure 49b).

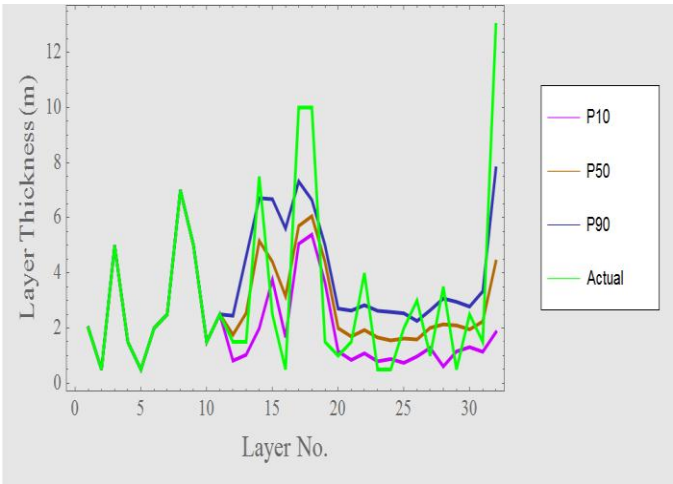

a)

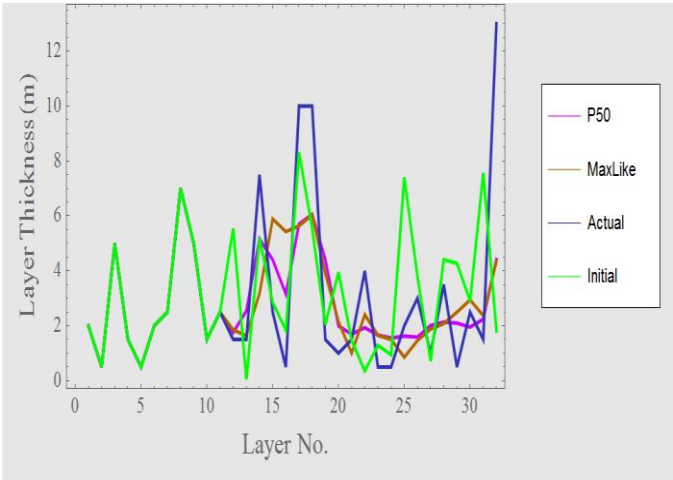

b)

Figure 49a). P10 (purple), P50 (yellow), P90 (blue), Actual phase velocities (green).

Figure 49b). Median P50 (purple), maximum likelihood (yellow), initial (green) and actual (blue) profiles of layer thicknesses.

The misfit problem of 10%, 50%, 90% probability (P10, P50, P90) with actual phase velocity profile is similar to the case shown in the (figure 51). The same problem occurs in the misfit between P50, maximum likelihood (Maxlike), initial upscaled phase velocities and actual profile. Also 15 m grid using Backus averaging was applied for upscaling.

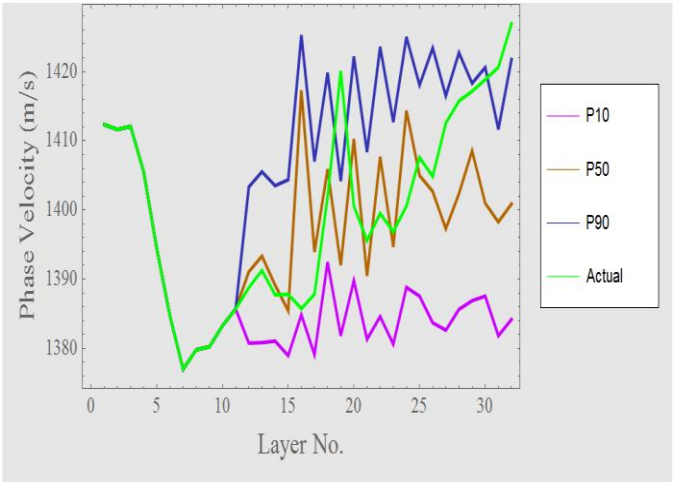

a)

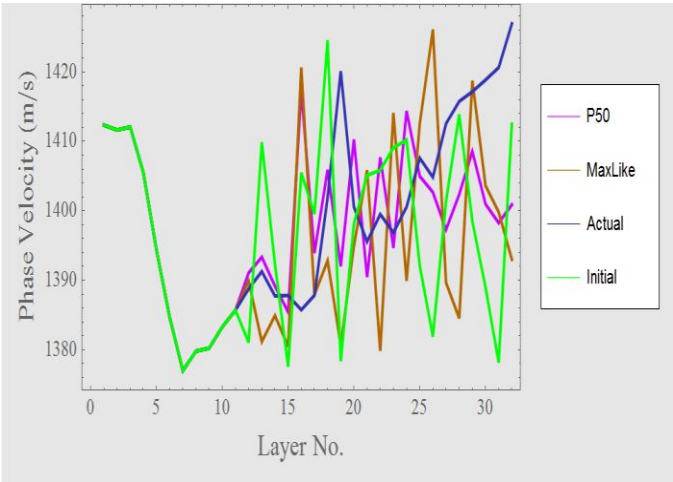

b)

Figure 51a). P10 (purple), P50 (yellow), P90 (blue), Actual phase velocities (green).

Figure 51b). Median P50 (purple), maximum likelihood (yellow), initial (green) and actual (blue) phase velocity profiles.

The plots for phase velocity versus depth look better for 10milion samples. Although no improvement is seen for the initial model, the maximum likelihood show a good approximation to the actual profile showing that increasing the number of iterations the random walker explore enough space (figure 52).

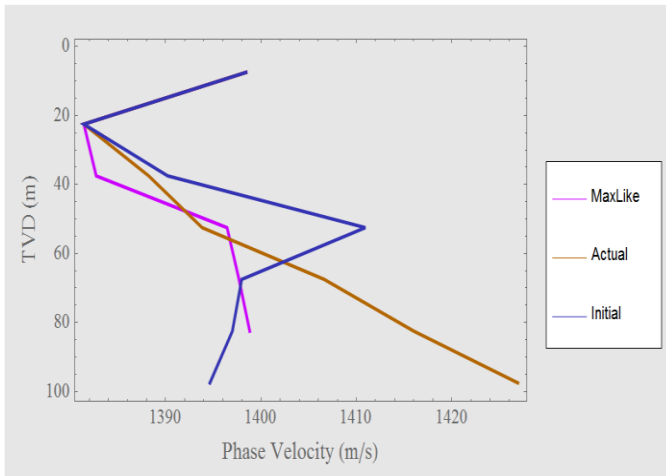

Figure 52. Maximum likelihood (purple), initial (blue) and actual (yellow) profiles of phase velocities

It is observed that the 10%, 50%, 90% probability (P10, P50, P90) profiles are well approximated after 10milion iterations. The P50 profile is closer to the actual compared to 1milion case and the P90 agree very well to the actual profile (figure 53).

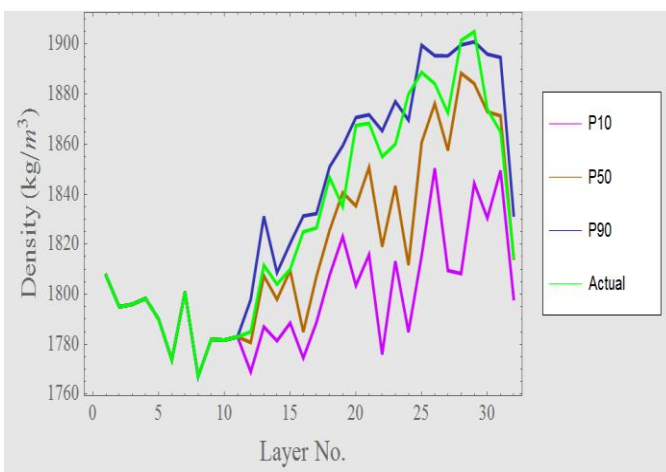

Figure 53. P10 (purple), P50 (yellow), P90 (blue) and actual density profiles

The fit is reasonably good between P50, maximum likelihood and the actual densities profile but the P50 is better approximated to the actual in the previous case. No improvement is attained for the initial model see (figure 54).

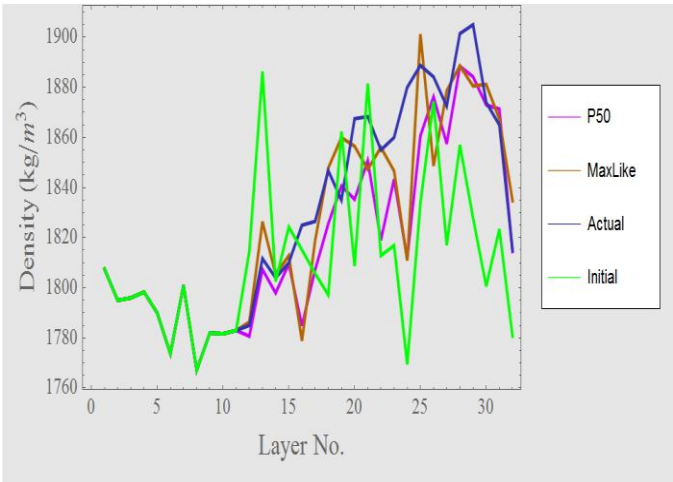

Figure 54. Median P50 (purple), maximum likelihood (yellow), initial (green) and actual (blue) density profiles

The density is plotted versus depth showing the maximum, initial and the actual density profiles. Again the inversion did not help to get the initial profile improved after moving from 1 to 10milion sampling points. It is not the case for maximum likelihood which significantly moves in the direction for excellent tight with the actual profile (figure 55).

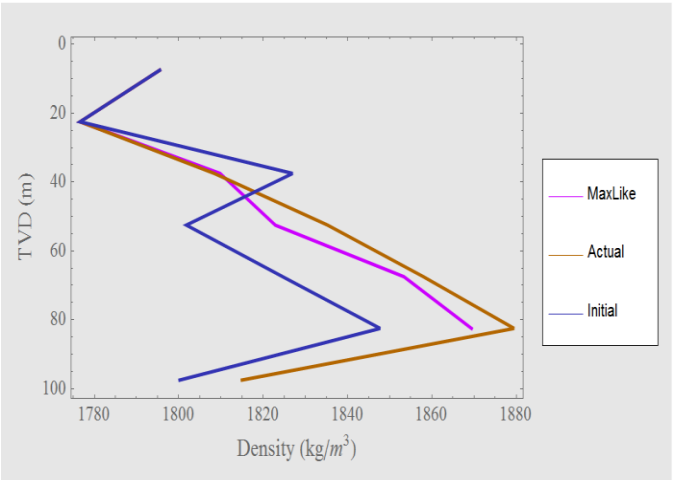

Figure 55. Maximum likelihood (purple), initial (blue) and actual (yellow) density profiles

The impedance plot gives a very good approximation seen in the 10%, 50%, 90% probability (P10, P50, P90) along with actual profiles. The maximum likelihood is well approximated to the actual and much better is the P90 with excellent tight with actual profile (figure 56).

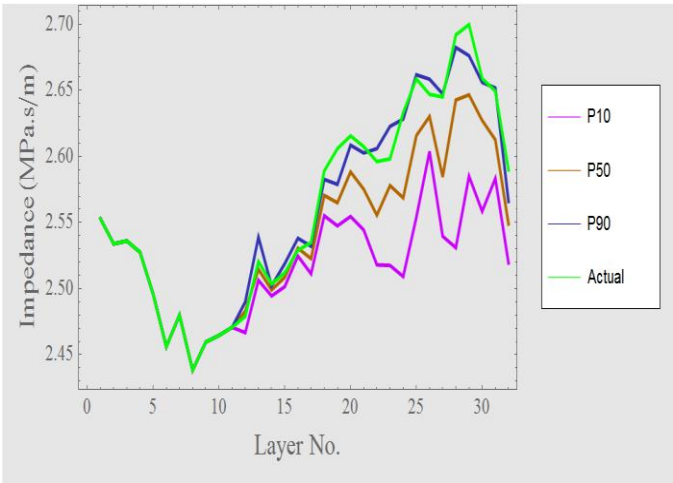

Figure 56. P10 (purple), P50 (yellow), P90 (blue) and actual impedance profiles

The P50 fit to actual profile is the same as that seen in the (figure 57). The maximum likelihood is well approximated to the actual. Once more the initial upscaled impedance is not improved by the inversion process.

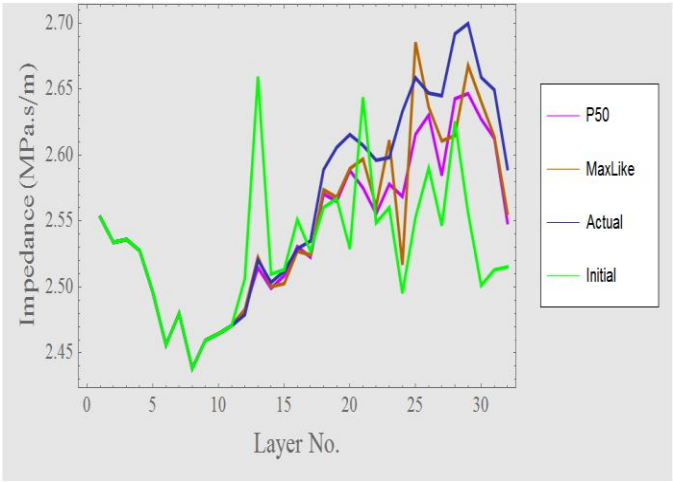

Figure 57. Median P50 (purple), maximum likelihood (yellow), initial (green) and actual (blue) profiles of impedance.

In the (figure 58) for impedance profiles is seen how well layer properties are estimated by fitting very well the maximum likelihood profile to the actual although the random walker is not improving the initial profile.

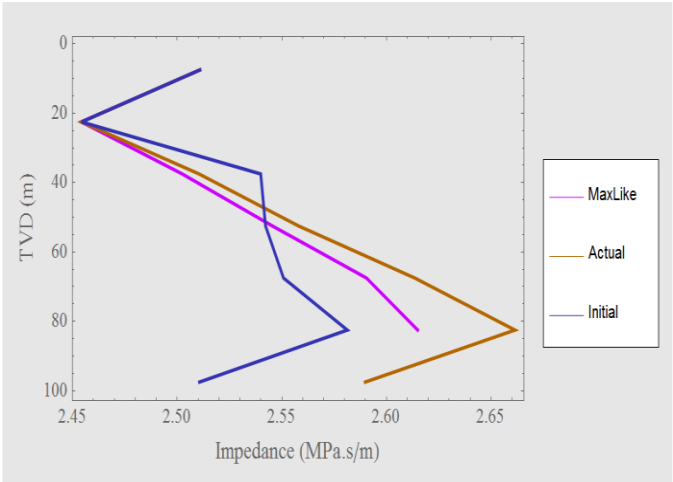

Figure 58. Maximum likelihood (purple), initial (blue) and actual (yellow) impedance profiles

The impedance profile versus depth gives a more detailed view showing how tight the profiles are to each other. Again despite of the inversion not have improved the initial model an excellent fit is obtained in the approximation of the maximum likelihood actual impedance profile (figure 59).

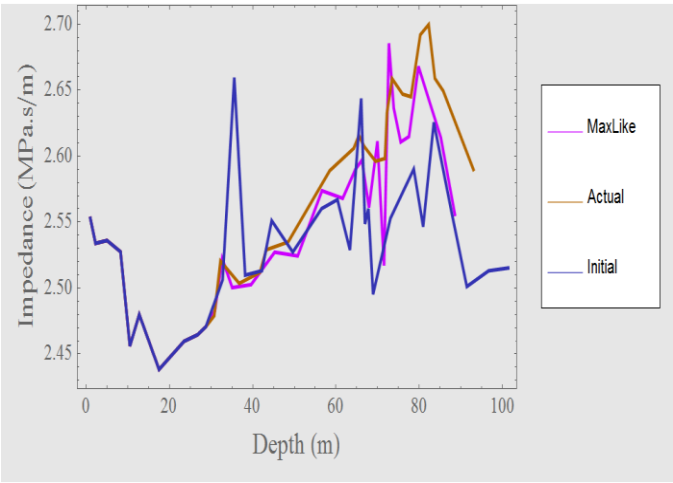

Figure 59. Maximum likelihood (purple), initial (blue) and actual (yellow) impedance profiles versus depth.

The pore pressure plot versus depth is obtained after moving the random walker in the region of model space for ten million samples which yield a promising result for solution of inverse problems. The fit among the curves show up as expected in a way to get an excellent prediction of the properties ahead of the bit. Finely a very good fit is clearly seen in the maximum likelihood to the actual impedance profile (figure 60).

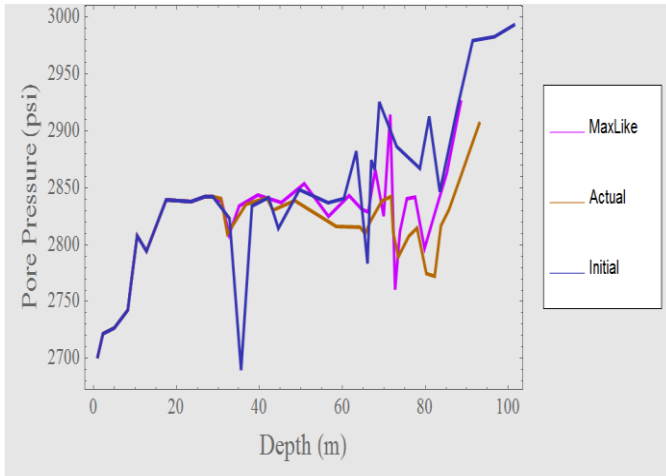

Figure 60. Median P50 (purple), maximum likelihood (yellow), initial (green) and actual (blue) pore pressure profiles.

The comparison of the results is shown in the (figure 61). A good fit is observed with 1milion samples figure. By moving the random walker to explore large space with ten million iterations the agreement between the maximum and the actual profile became excellent which indicate that if more samples are drawn by increasing the number iterations the fit might improve much better.

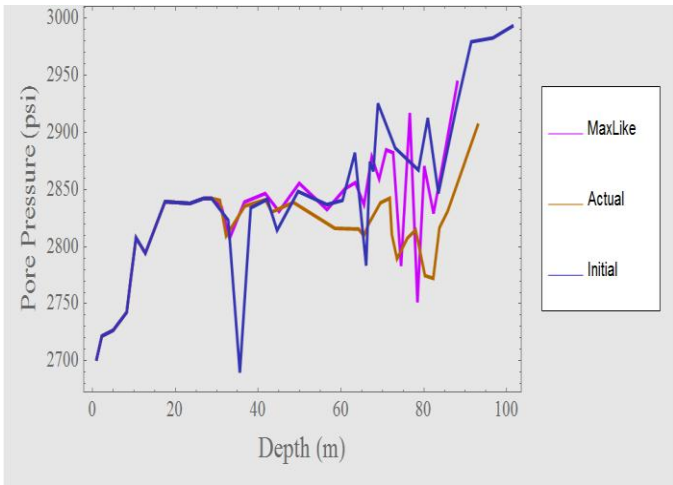

a)

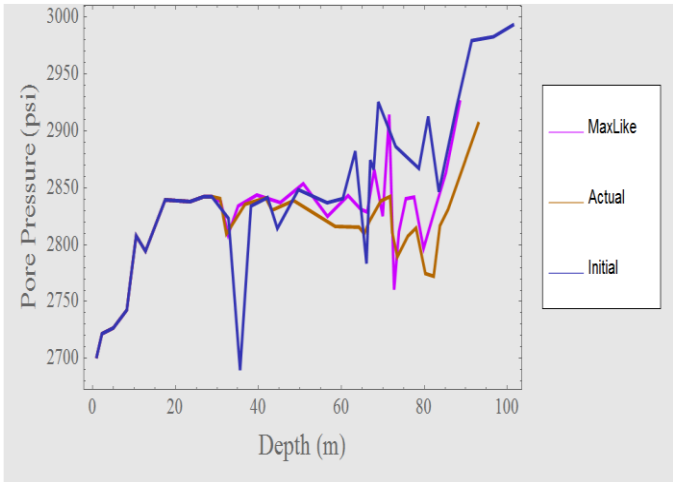

b)

Figure 61a). Median P50 (purple), maximum likelihood (yellow), initial (green) and actual (blue) pore pressure profiles.

5. Discussion

In this section is discussed the results of simulations obtained by running the inversion code which are the posterior probability of the parameters (layer thickness, velocity and density).

The inversion is carried out following the bivariate distribution of layer thicknesses. This type of layer distribution is characterised by two variable. This distribution was chosen because it represents a stronger constrain on the layer thickness distribution (figure 12).

The analysis started with two and three layer cases which illustrated the capability to solve for or detect thin layer ahead of the bit. By playing with the code it was observed that decreasing the thicknesses of the layers the resolution to capture thin layers decreased because of low frequency content. Similar problem occurred when high frequency content was cut off by high dapping effect in the signal. As consequence the layer interfaces in brown yellow dots shift from corresponding wave form. To handle with this problem high frequency signal should be used or the dapping effect should be reduced which means the quality factor should be increased. The minimum layer thicknesses detected from synthetic seismogram of up-going wave after firing a seismic source is 0.1m. The resolution of synthetic seismogram from Ricker wavelet source decreased to 4.5m because the Ricker wavelet effect removed high frequency content in the impulse seismic signal (figure 20).

The analysis of two layer case was continued by inverting for the properties ahead of the bit from synthetic seismogram of up-going wave obtained by firing a perfect seismic source. The Relation of the two-way travel-time and the reflection coefficient with layer properties yield one equation relating the thickness of the layers to the velocity and the two-way travel-time and the reflection coefficient to acoustic impedance. The problem was assumed to be non-unique due to the fact that it contained 2 equations and 6 unknown. Constrain was applied to the solution by assuming that the parameters of the first layer were known (h1, v1 and density1). The equation for reflection coefficient was left with two unknowns parameters. It is important to note that from reflection coefficient equation it was not possible to solve for v2 and density2 but it was for acoustic impedance in the second layer which was a breakthrough. For the two-layer case, the solution for the synthetic seismogram assumed that the thickness of

the second layer was infinite. Nevertheless, it did not generate a reflection at the bottom of the second layer. The solution was constrained by adding a third layer which generated a reflection between the second and third layer resulting the second equation that related the thickness of the layer (h2) to the velocity (v2) and the two-way travel-time (t2) which was used to solve for density 2 and v2 for the second layer.

In this thesis a complex problem was studied by looking at 100m column depth ahead of the bit which corresponded to 32 layers, 62 equations and 96 unknown parameters (figure 28). The inversion code assumed that the bottom layer had an infinite thickness, so it was not possible to get the relation of the thickness of the layer (h32) to the velocity (v32) and the two-way travel-time (t32). It was left 31 equations relating the layer thicknesses to the velocities and travel times and 31 equations for the reflection coefficients. As an ill-posed inverse problem was obtained, constrain was applied by assuming that it was known the parameters for 30 column depth that corresponded to 11 layers and 33 known parameters. It was left 21 equations for the reflection coefficients starting at the interface between layer 11 and layer 12 and 20 equations relating the layer thickness to the velocity and travel time (figure 29). Again the code assumed that the bottom layer had an infinite thickness so, no reflection was produced at the base of the 100 m column. Note that by using 21 equations for the reflection coefficients it was not possible to solve for density and velocity separately but it was for impedance from layer 12 to layer 32. In addition to getting 21 unknown impedances parameters, it was possible to solve 20 equations relating the layer thicknesses to velocities and travel times to get velocities from layer 12 to layer 31. As stated previously, it was not possible to get v32 because the equation that relates the layer thickness to velocity and travel-time for layer 32 was not applied. At this stage the solution obtained for the inversion code was still non-unique figure 34. This was the reason why the inversion did not recover the layer properties and the Ricker wavelet source complicated the problem even further because it cut off high frequency information which prevented resolution of thin layers and low frequency information which removed low frequency trends from the synthetic seismogram. Attenuation effect further complicated the problem by damping out the signal from deeper layers (figure 29). A statistical constrain was applied to 21 layer thicknesses inverse problem. The problem still was non-unique but constrained within certain boundaries. In practice it is not ever known the layer thicknesses below the bit. It is relied on statistical information from offset

wells. As stated previously, if it is statistically constrained the layer thicknesses, the solution will still be non-unique but should be constrained within certain boundaries (figure 29).

6. Future improvements

- For current inverse problem the lithology of the layers were assigned by computing sand and shale index to simplify the inversion problem, for a more realistic analysis it is recommended to include in the estimation of parameters the inversion for lithology and attenuation effect.

- The simulations were carried out starting with 1milion sample, which is not enough to produce acceptable result as the random walker will not explore sufficiently the region of the model space. It was observed an excellent improvement on the plots after increasing the samples from 1 to 10milion which make sense because the algorithm, compute the best solution provided that enough samples are generated. As no more than 10milion iterations were generated due to machine memory limitations, a better improvement should be obtained by increasing the sampling points.

7. Conclusion

The simulations of a well data from the field performed in this thesis using Walfram mathematica software, produced results that unable to draw the following conclusion:

- Bayesian theorem along with metropolis algorithm which generated samples from likelihood probability provided the solution for the inverse problem. The properties of the layers (layer thicknesses, velocities and densities) ahead of the bit were estimated from borehole seismic data.

- Pore pressure was predicted by using the impedance as input to Bower's equation. The overburden was computed from predicted densities.

- The parameters were predicted theorically. I practice when drilling a well, it is not ever known the layer thicknesses below the bit. Statistical information from offset set wells is the only source to understand the layer thicknesses distribution. If the layer thicknesses are statistically constrained the solution will still be non-unique but it should be constrained within certain bowndareis.

- For the current inverse problem, adding the inversion of attenuation effect, multivariate layer thicknesses distribution, lithology distribution in the layers, overpressure causes which demanded laboratory test should increase the complexity of the problem but in turn it should probably narrow the range of the uncertainty which should give more consistency in the solution of the ill posed inverse problem. That would be strong support for engineering application.

- The simulations were carried out starting with 1milion sample, which is not enough to produce acceptable result as the random walker will not explore sufficiently the region of the model space. It was observed an excellent improvement on the plots after increasing the samples from 1 to 10milion which make sense because the algorithm, compute the best solution provided that enough samples are generated.

- The maximum samples generated in the simulation for the inversion process is 10milion. No more than this number was possible to compute due to low capacity of the machine memory. The improvements on the results after increasing the number of samples suggest that a machine with bigger memory should help to provide a better solution.

Nomenclature

$\mathbf{c_i}$	Phase velocity of layer i
c(w)	Phase velocity
$\mathbf{C_0}$	Reference phase velocity
$\mathbf{d_i}$	Thickness of layer i
$\mathbf{D_i(w)}$	Fourier transform of downgoing wave of the top layer i.
$\frac{\mathbf{dT}}{\mathbf{dZ}}$	Derivative travel-time as function of depth
g	Gravity acceleration.
$\mathbf{h}$	Layer thickness, m
ho	Hydrostatic column height
$\mathbf{I_p}$	Acoustic impedance
m	Model parameter.
$\mathbf{P_h}$	Hydrostatic pressure.
$\mathbf{P_p}$	Subnormal pressure.
P	Pore pressure
p(m, I)	Posterior probability of the parameters.
p(m, I)	Posterior probability of the parameters.
$\mathbf{Q'(w)}$	Quality factor
$\mathbf{Q_0}$	Reference quality factor
$\mathbf{r_i}$	The reflection coefficient of the interface between layers i and i+1.
$\mathbf{R_o}$	Reflection coefficient at the surface for a downgoing wave.
$\mathbf{R_i}$	Reflection coefficient of layer i
S	Overburden
$\mathbf{t_d}$	Direct travel times, mS
T(H)	Traveltime, mS

$\mathbf{U_i(w)}$	Fourier transform of upgoing wave of the top layer i.
$\mathbf{v_0}$	Velocity at the top of the layer, m/s
$\mathbf{v_{01}}$	Velocity of unconsolidated fluid-saturated sediments
V(H)	Velocity of layer thicknesses, m/s
V(z)	Velocity of depth after inversion, m/s
$\mathbf{X(w)}$	Fourier transform of a synthetic seismogram.
$\mathbf{Y_{i+1}}$	The ratio of the spectrum of upgoing and downgoing waves for the bottom layer
$\mathbf{W}$	Angular frequency
$\mathbf{W_0}$	Reference angular frequency
$\mathbf{Z_i}$	The acoustic impedance of ith-layer, Kg/$\mathbf{m^2}$s
$\boldsymbol{\alpha}$	Absorption coefficient
$\boldsymbol{\alpha 1}$ and β	Constants that control the variation in velocity with effective stress
$\boldsymbol{\Phi}$	Porosity
$\boldsymbol{\Upsilon}$	Constant.
$\boldsymbol{\rho_b(z)}$	Bulk density
$\boldsymbol{\rho_f}$	Fluid density
$\boldsymbol{\rho_m}$	Fluid density

References

1. Arroyo, J.L., Brenton, P., Dijkerman, H., Dingwall, S., Guerra, R., Hope, R., Williams, H.B.M., Jimenez, R.R., Tulett, L.J., Leaney, S., Lim, T.k., Menkiti, H.,Tcherkashnev, P.S., Burg, T.T., Veliac, M., *Superior Seismic Data from the Borehole.* 2003.
2. Malinverno, A., Haldorsen, J.U., Prange, M., Borland, W.H., *Bayesian Inversion of First Arrival Travel times and Waveform Data In a Zero-offSet Vertical Seismic Profile.* 2009.
3. Birchwood, R., *Gas hydrate crystal structure.* 1997.
4. David, K.R., *Use of Zero-Offset Seismic-While-Drilling Data for Improving Velocity Prediction Ahead of the Bit*. 2014. p. 38.
5. Stunes, S., *Methods of Pore Pressure Detection from Real-time Drilling Data*. 2012, Norwagian University of Science and Tectnology. p. 110.
6. Rabia, H., *Well Engineering and Construction.* 2002.: p. 789.
7. Kennett, P., Ireson, R.L., and Conn, P.J., *Vertical seismic profiles: Their Application in Exploration Geophysics.* Geophysical Prospecting., 1980. **28**: p. 676-699.
8. Solano, G.E., *Zero offset VSP data processing and attenuation estimates in the oil sands.* 2004, University of Alberta. p. 110.
9. Geoff, J.M.M., William, P.C., Michel, D.K., and Warren, B., *VSP traveltime inversion: Near-surface issues.* Geophysics, 2004. **69**: p. 345-351.
10. Bolmer, R.T., Buffer, H., Hoskins, R.A., Stephen., and Swift, S.A. *Vertical Seismic Profile At Site 765 And Seismic Reflectors In The Argo Abyssal Plain1.* in *Ocean Drilling Program*. 1992.
11. Brewer, R.J., *The Look Ahead VSP Survey: Its Utility and Future.* 2002.
12. Lizarralde, D., and Swift, S., *Smooth inversion of VSP travel time data.* Geophysics, 1999. **64**: p. 659-661.
13. Stewart, R.R., *VSP interval velocities from traveltime inversion.* Geophysical Prospecting., 1984. **32**: p. 608 – 628.
14. Duijndam, A., *Detailed Bayesian inversion of seismic data.* 1987.
15. Galey, D.C., *A method of calculating synthetic seismogram which include the effects of absorption and dispersion.* 1981.
16. Mosegaard, K., Tarantola, A., *Probabilistic Approach to Inverse Problems. .* 2002.
17. Argoul, P., *Overview of the inverse Problems.* 2012.
18. Glickman, M.E., and Van, A.D. , *Basic Bayesian methods.* 2007.
19. Mouchet, J.P., Mitchell A., *Abnormal Pressures While Drilling: Origins, Prediction, Detection, Evaluation.* 1989. 255.
20. Dutta, N.C., *Geopressure prediction using seismic data.* Geophysics, 2002. **67**: p. 2012–2041.
21. Bowers, L.G., *Pore Pressure Estimation from Velocity Data: Accounting for Overpressure Mechanisms besides under compaction.* 1995.
22. Mukerji1, T., *Seismic Detection And Estimation Of Overpressures.* 2002: p. 21.
23. Kotz, S., Balakrishnan, N., & Johnson, N.L. , *Continuous Multivariate Distributions.* 2000. **1**.